Electronic Supplementary Information for

Introducing halogen-bonded gates in zeolitic frameworks for efficient benzene/cyclohexene/cyclohexane separation

Zi-Jun Liang,[‡] Fang-Di Dong,[‡] Le Ye, Kai Zheng, Ding-Yi Hu, Xi Feng, Wen-Yu Su, Zhi-Shuo Wang, Mu-Yang Zhou, Zi-Luo Fang, Dong-Dong Zhou,* Jie-Peng Zhang,* and Xiao-Ming Chen

MOE Key Laboratory of Bioinorganic and Synthetic Chemistry, School of Chemistry, GBRCE for Functional Molecular Engineering, IGCME, Sun Yat-Sen University, Guangzhou 510275, China

[‡] These authors contributed equally to this work.

* Corresponding Authors: zhoudd3@mail.sysu.edu.cn; zhangjp7@mail.sysu.edu.cn

Experimental Procedures

Materials and Methods. All reagents were commercially available and used without further purification. [Zn(mtz)$_2$] (MAF-7, Hmtz = 3-methyl-1,2,4-triazole) was synthesized according to the literature method.[1] Elemental analyses (EA) were performed by a Vario EL elemental analyzer. Powder X-ray diffraction (PXRD) were collected using a SmartLab X-ray powder diffractometer (Cu Kα) at room temperature. [1]H-nuclear magnetic resonance (^{1}H-NMR) spectra were recorded on a Bruker BioSpin GmbH (400 MHz). Thermogravimetry (TG) analyses were carried out on a TA Q50 system under N$_2$ flow with a heating rate of 10 ℃ min^{-1}. Differential scanning calorimetry (DSC) measurements were on a TA DSC 250 instrument. Attenuated total reflection Fourier transform infrared spectroscopy (ATR−FTIR) experiments were performed on a PerkinElmer Frontier. Raman spectra were obtained by a Renishaw inVia (532 nm). Solid-state ^{13}C-nuclear magnetic resonance (^{13}C-NMR) spectra were recorded on a Bruker Ascend (600 MHz). Vapour sorption isotherms were measured with collected by a BSD-VVS&DVS gravimetric adsorption analyzer (Beishide Instrument Technology (Beijing) Co., China). Before the sorption experiment, samples were activated under high vacuum at 393 K for 3 hours.

Synthesis of [Zn(btz)$_2$] Guest. 3-Bromo-1,2,4-triazole (Hbtz, 59.2 mg, 0.4 mmol) and Zn(NO$_3$) 6H$_2$O (59.5 mg, 0.2 mmol) were dissolved in *N,N*-dimethylformamide (DMF, 2 mL), then transferred into a 15-mL glass container with Teflon cap and heated at 373 K for 24 hours. After slowly cooling down to room temperature, colourless rhombic dodecahedral single crystals were obtained after filtration. For the microcrystalline sample: Hbtz (1.18 g, 8 mmol) and Zn(NO$_3$)$_2$ 6H$_2$O (1.19 g, 4 mmol) were dissolved in DMF (20 mL) in a glass vial, and sealed to stir at 373 K for 24 hours. Subsequently, white powder (1.45 g, yield ~83%) was filtered, washed with methanol, and dried in air. EA calcd (%) for Zn(C$_2$N$_3$HBr)$_2$(C$_3$N$_3$H$_7$O)$_{0.4}$(CH$_4$O)$_{0.6}$: C, 17.08; H, 1.78; N, 21.98. Found: C, 17.15; H, 1.64; N, 21.97.

Single-crystal X-ray Diffraction (SCXRD) Measurements

Diffraction data were collected on a XtaLAB Synergy Custom single-crystal diffractometer by using graphite monochromated Cu-Kα radiation. Absorption corrections were applied by using multi-scan program *CrysAlisPro*. The structures were solved with the direct methods and refined with a full-matrix least-squares technique with the SHELXTL program package. Anisotropic thermal parameters were applied to all non-hydrogen atoms. The hydrogen atoms were generated by the riding mode. CCDC 2386982–2386983 contains the crystallographic data. These data are provided free of charge by the joint Cambridge Crystallographic Data Centre via www.ccdc.cam.ac.uk/data_request/cif. Single-crystal data and details of refinements were summarized in Table S1.

Continuous Adsorption-Desorption Cycle Experiments

The activated sample (*ca*. 200 mg) was placed in a glass vial (20 mL), then pure Bz or equimolar mixture of Bz/Cya/Cye (15 mL) was immediately injected into the glass

vial, then sealed and kept in an oven at 313 K. Considering the factors of adsorption kinetics, the sample was fully soaked in the mixed solution (5 h), then filtered, and purged with N_2 flow (20 mL min^{-1}) at room temperature for 10 minutes to remove the solvent on the surface. Then the sample was filtered for further analysis. To analyze all the adsorbates in the sample, partial sample (*ca.* 40 mg) was digested using DCl (0.1 mL, 20% DCl in D_2O), followed by the addition of CD_3OD (0.5 mL) for NMR analysis. The remaining sample (without digestion) was heated at 393 K for 2 hours under vacuum for the next adsorption process, which was used for repeating the above operations of adsorption in pure Bz or Bz/Cya/Cye mixtures and desorption for four consecutive adsorption-desorption cycles.[2]

Gas Chromatography Analyses
The activated sample (*ca.* 200 mg) was placed in a glass vial (20 mL), then the equimolar mixtures of Bz/Cya, Bz/Cye or Bz/Cya/Cye (10 mL) were immediately injected into the glass vial, then sealed and kept in an oven at 313 K. After 5 hours, the sample was filtered and purged with N_2 flow (20 mL min^{-1}) at room temperature for 10 minutes to remove the solvent on the surface. Then the sample was filtered for further analysis. In order to analyze all the adsorbates in the sample, the sample was digested using hydrochloric acid (0.1 mL, 12 M), and extracted by *n*-hexane (0.2 mL) for three times, then the *n*-hexane extractions were combined (0.6 mL) for GC.[2,3]

The Bz/Cya, Bz/Cye or Bz/Cye/Cya ratios in the digestion solutions were analyzed on a Shimadazu 2014C gas chromatography (GC) system with an Agilent CP Sil 5 CB chromatographic column and an FID detector. For each GC injection, 1 μL aliquot of analytes were injected in manual. The front injection temperature was 150 ℃. After injection, the oven temperature was held at 35 ℃ for 5 min.

The purity (p_i) of component i was calculated by:

$$p_i = \frac{C_i}{C_1 + \cdots + C_i} \times 100\%$$

where C_i was the concentration of component i obtained through standard curves on GC.

The selectivity (S) was calculated by:[4]

$$S = \frac{C_2/(C_1 + \cdots + C_i - C_2)}{C_2'/(C_1' + \cdots + C_i' - C_2')}$$

where C_i' was the concentration of component i in the blank sample (equimolar mixtures) obtained through standard curves on GC.

Standard curves on GC. Different concentrations of *n*-hexane solution containing Bz, Cye and Cya were used to set the standard curves for GC measurements. The concentration of the components (mol L^{-1}) and final standard curves are listed below (Fig. S34).

Calculation of Diffusional Rate Constant

The diffusional rate constant B was employed by the short-time solution equation presuming a step change in adsorption:[5,6]

$$\frac{q_t}{q_\infty} = \frac{6}{\sqrt{\pi}} \times \sqrt{\frac{D}{r^2} \times t}$$

$$B = \frac{D\pi^2}{r^2} = \frac{(\frac{q_t}{q_\infty})^2 \times \frac{\pi^3}{36}}{t}$$

where q_t is the gas uptake at time t, q_∞ is the theoretical gas uptake at equilibrium, D is the diffusivity and r is the radius of the equivalent spherical particle.

Computational Simulations

All simulations/calculations were performed using the Materials Studio 5.5 package. The guest adsorption was generated from grand canonical Monte Carlo (GCMC) simulations with the fixed loading task at 298 K in the Sorption module. For GCMC simulations, the Metropolis method and universal force field (UFF) was used. All the charge of atoms were adopted Mulliken charges, which were calculated from periodic density functional theory (PDFT), and the cutoff radius was chosen as 18.5 Å for the Lennard-Jones (LJ) potential. The electrostatic interactions and van der Waals interactions were handled using the Ewald and Atom based summation methods, respectively, and all the equilibration steps and production steps were set as 1×10^7.

Due to the difficulty in establishing an accurate model of the "amorphous" state of the framework, we simulate the transient structural transformation of the guest as it passes through the aperture to observe the locally aperiodic behavior by using the periodic framework as the initial structure.

PDFT calculations were performed by the Dmol^3 module. All geometry optimizations adopted the generalized gradient approximation (GGA) with the Perdew-Burke-Ernzerhof (PBE) functional and the double numerical plus d-functions (DNP) basis set, grimme for DFT-D correction, and the Effective Core Potentials (ECP).[7-9] The energy, gradient and displacement convergence criteria were set as 1×10^{-5} Ha, 2×10^{-3} Å and 5×10^{-3} Å, respectively. The host framework and the guest molecule were both regarded as flexible, and the adsorption enthalpy (ΔE_{ads}) were calculated by $\Delta E_{ads} = E_{host+guest} - E_{host} - E_{guest}$ (the E_{host} and E_{guest} are the energies of the host and guest respectively).[10]

Molecular dynamics (MD) simulations were performed in the Forcite module. The initial configurations for the MD simulations were produced by the GCMC loading results followed with global geometry optimizations through the universal forcefield. All of the MD processes adopted the canonical ensemble with constant volume/temperature (NVT) using Nose thermostat and random initial velocities. The time step was 1.0 fs and total simulation time was 5 ns. The electrostatic interactions and the van der Waals interactions were evaluated by the Ewald summation method, with a Buffer width of 0.5 Å. The first 2 ns were used as equilibrium and the

following 2 ns were adopted for statistical analysis such as for mean square displacements.
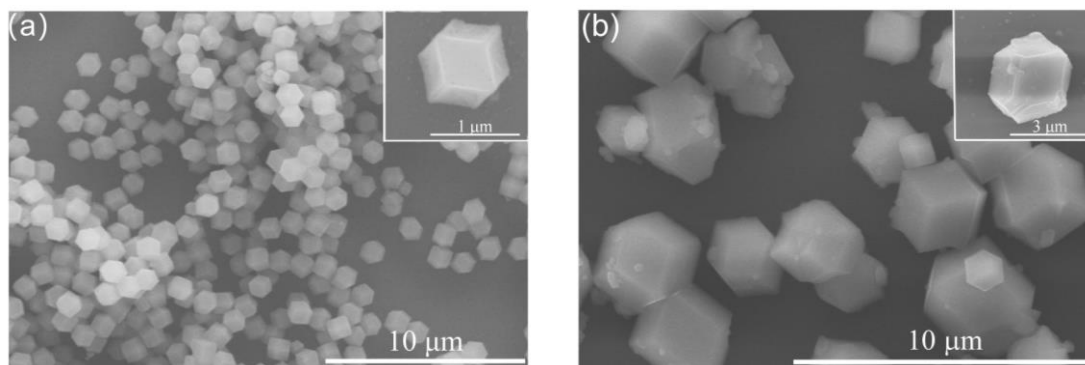
Fig. S1 SEM images of (a) MAF-7Br and (b) MAF-7.
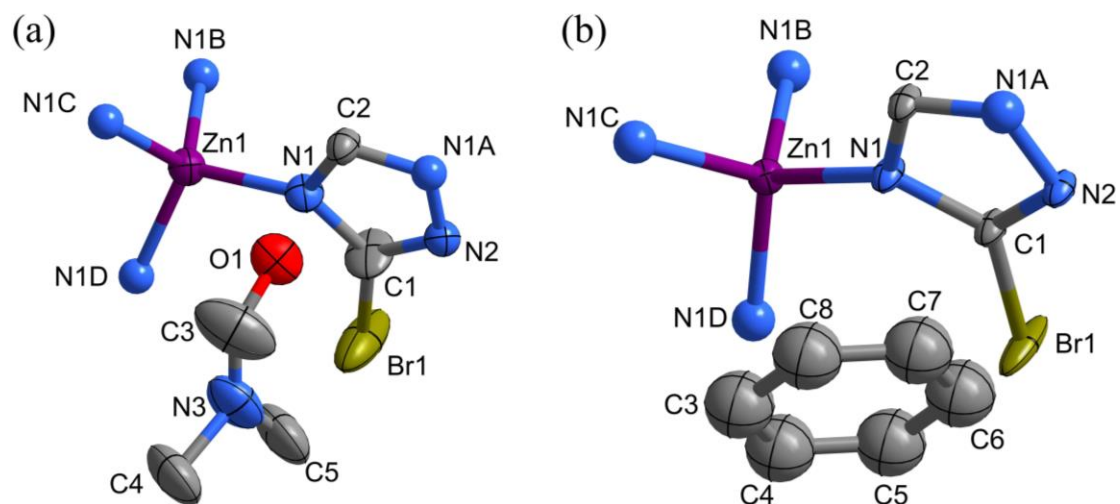
Fig. S2 The coordination environments in (a) MAF-7Br and (b) Bz@MAF-7Br. Symmetry codes: A = x, 1–z, 1–y; B = 3/2–y, –1/2+x, –1/2–z; C = 1–x, 2–y, z; D = –1/2+y, 3/2–x, –1/2–z. Hydrogen atoms are omitted for clarity.
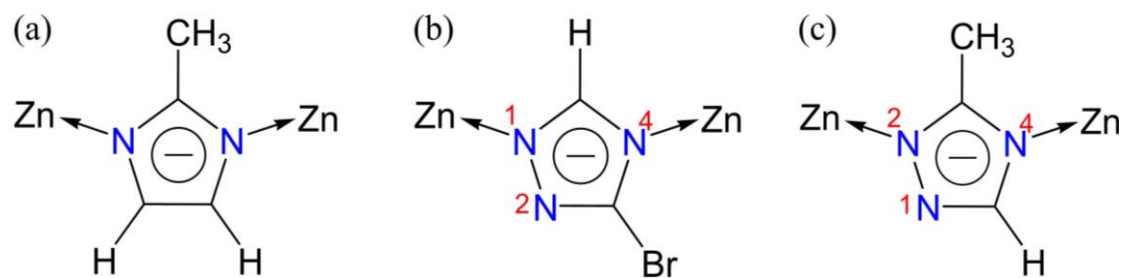
Fig. S3 The different coordination modes of the azolate ligands in (a) MAF-4, (b) MAF-7Br, and (c) MAF-7.
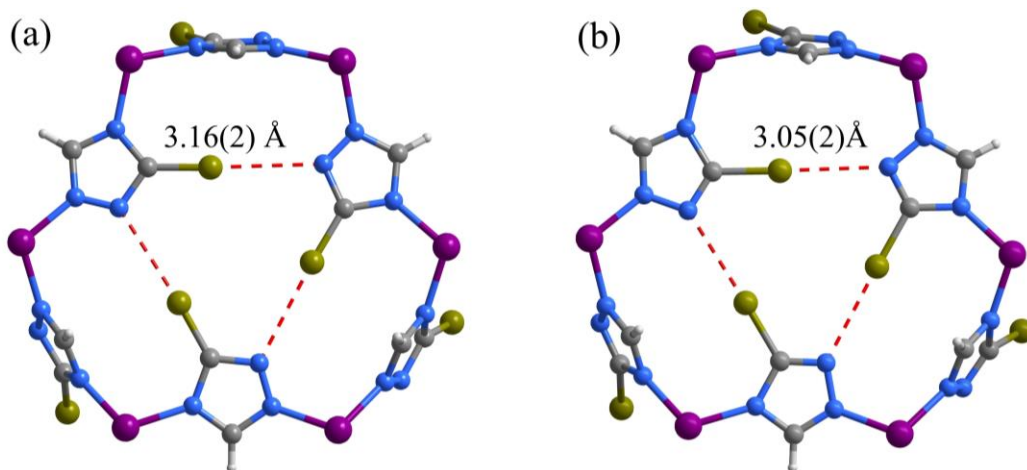
Fig. S4 The 6MR apertures in (a) MAF-7Br and (b) Bz@MAF-7Br, the halogen bonds are shown with red dashed bonds.
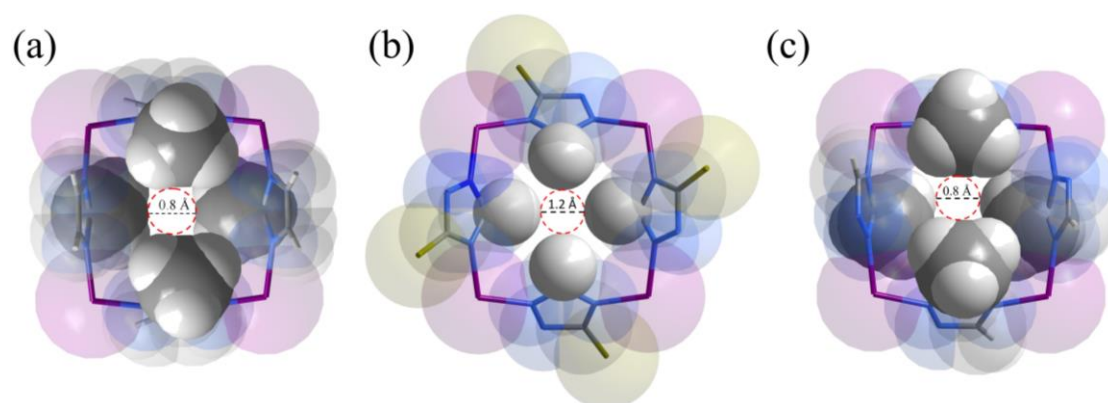
Fig. S5 The 4MR apertures in (a) MAF-4, (b) MAF-7Br, and (c) MAF-7, the functional groups (–H or –CH$_3$ groups) blocking the apertures are highlighted in the space-filling mode without transparency.
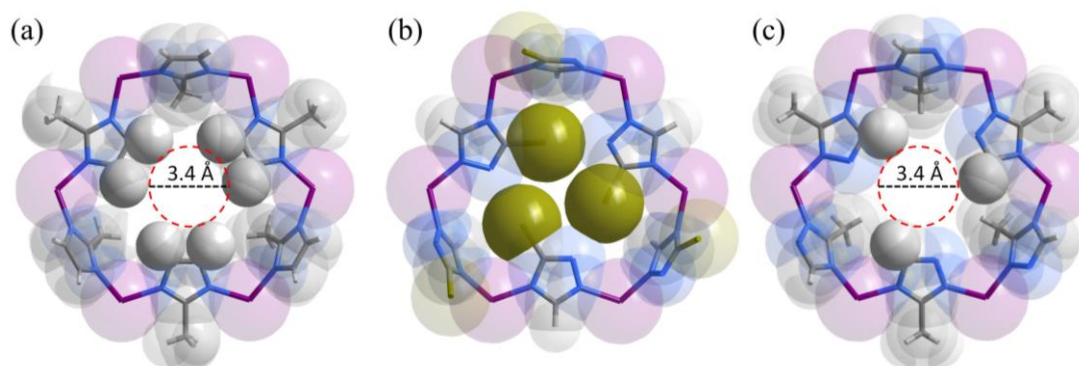
Fig. S6 The 6MR apertures in (a) MAF-4, (b) MAF-7Br and (c) MAF-7, the functional groups (–H or –CH$_3$ groups) blocking the apertures are highlighted in the space-filling mode without transparency.
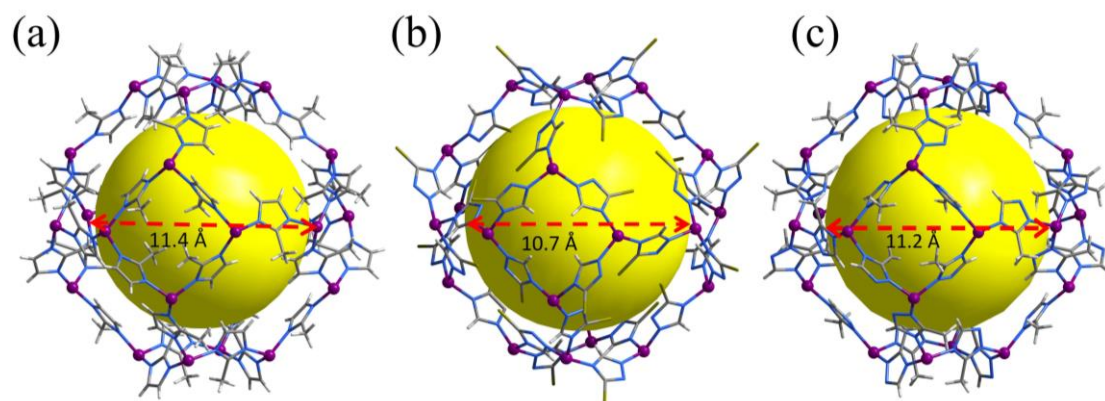
Fig. S7 The pore cavities (yellow ball) in (a) MAF-4, (b) MAF-7Br, and (c) MAF-7.
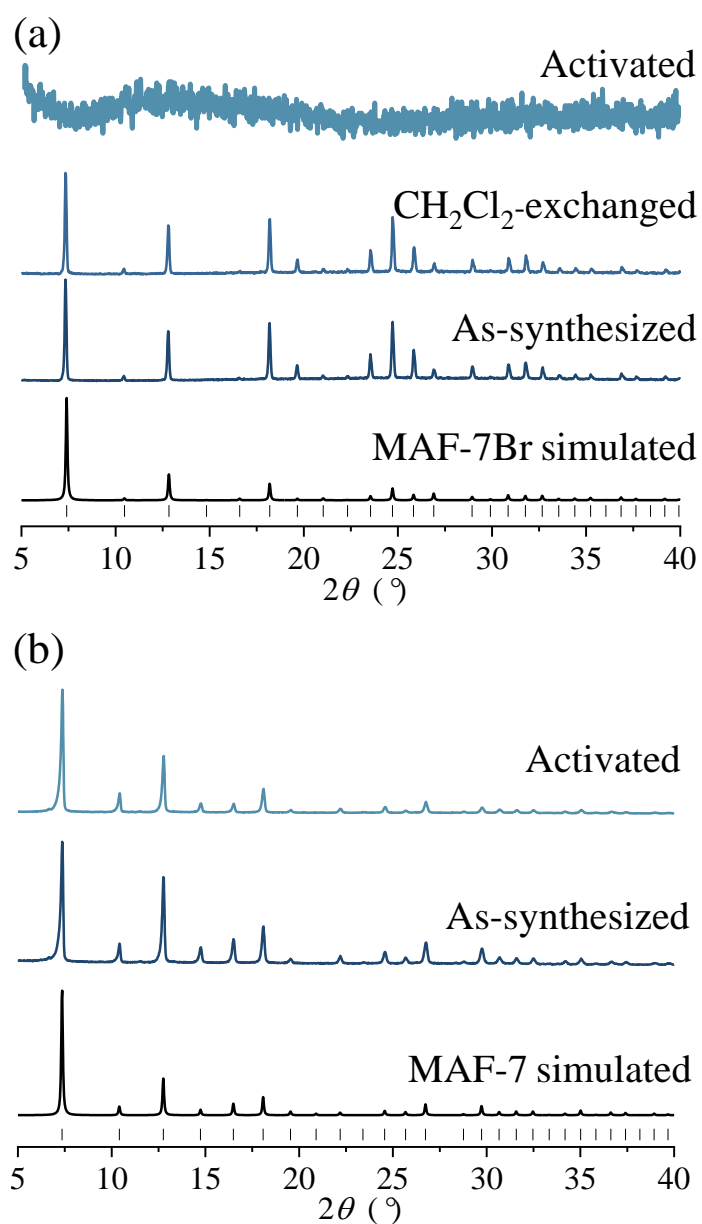
Fig. S8 PXRD patterns of (a) MAF-7Br and (b) MAF-7.
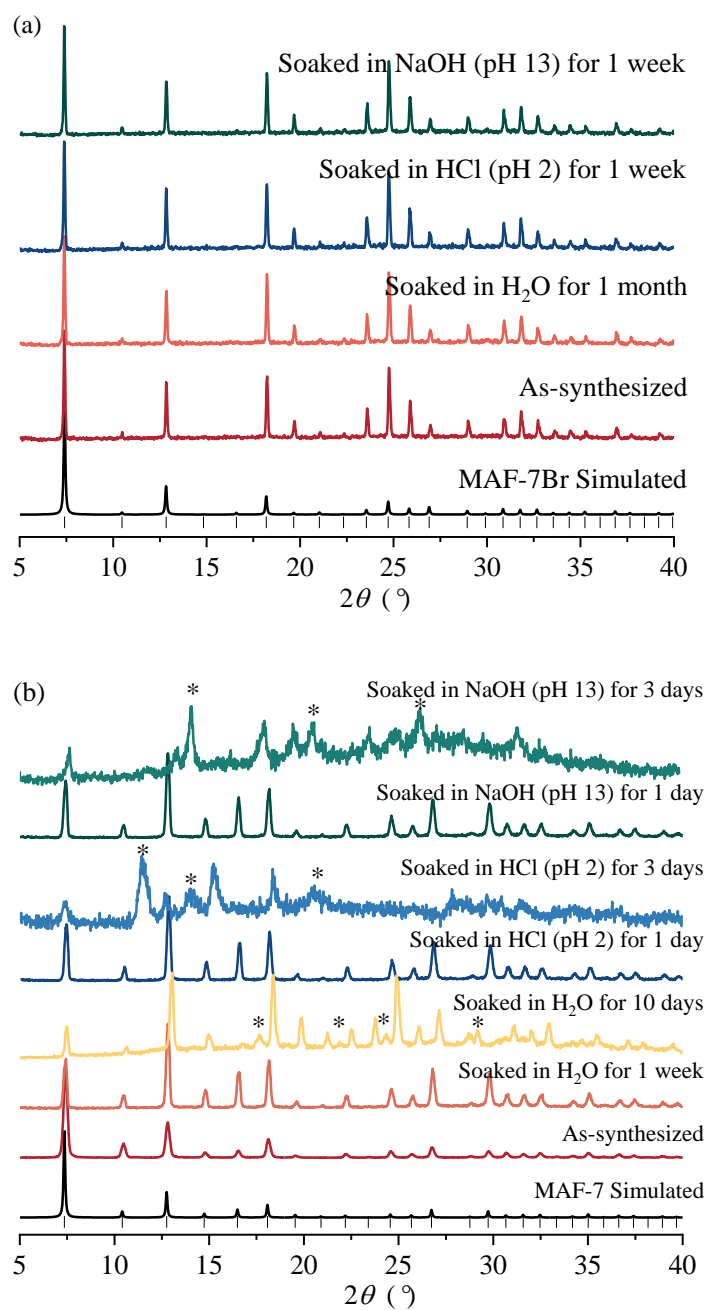
Fig. S9 PXRD patterns of (a) MAF-7Br (b) MAF-7 at different conditions. Asterisks represents unknown impurity.
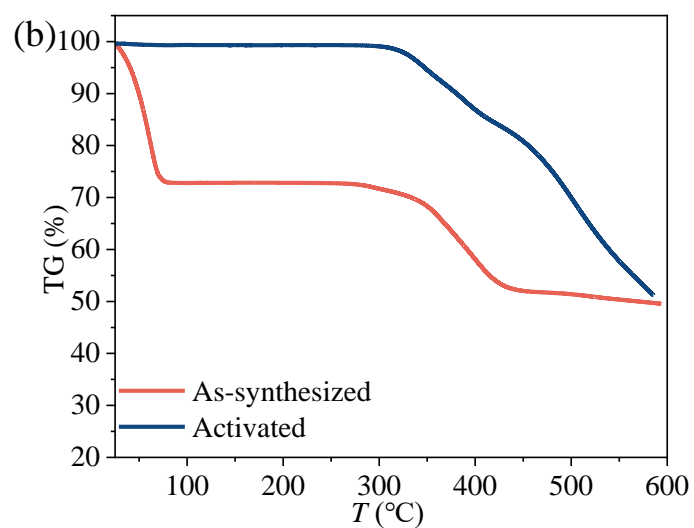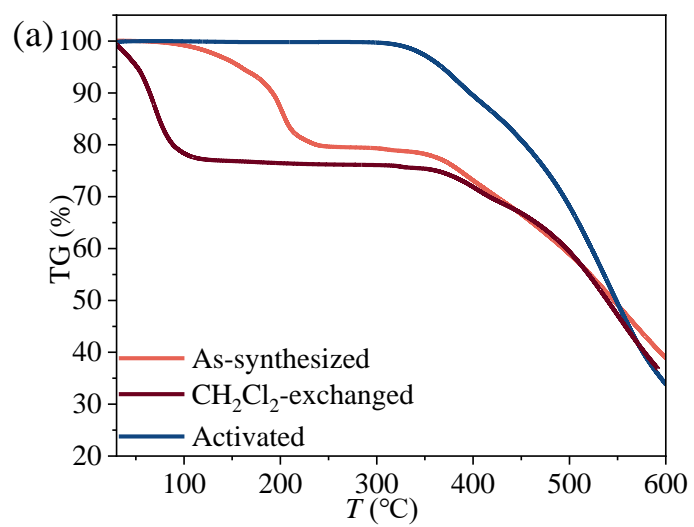
Fig. S10 TG curves of (a) MAF-7Br and (b) MAF-7 with different treatments.
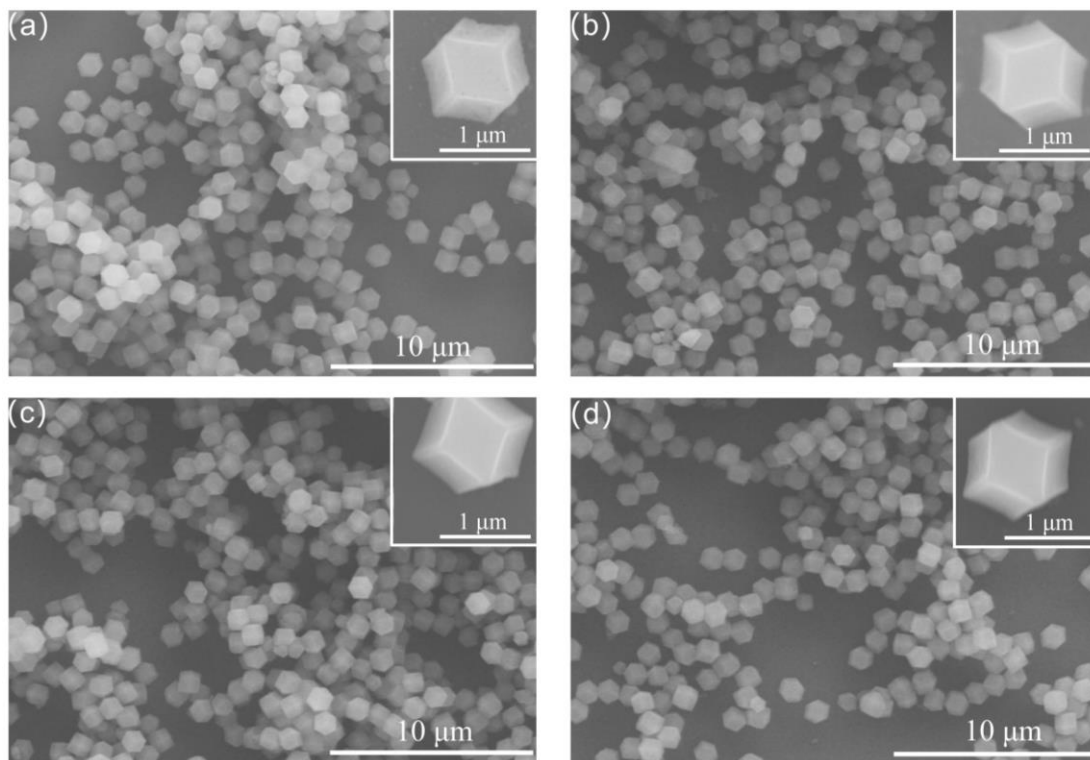
Fig. S11 SEM images of (a) as-synthesized and (b) activated samples of MAF-7Br, and (c,d) activated MAF-7Br samples soaked in Bz (c) and DMF (d), respectively.
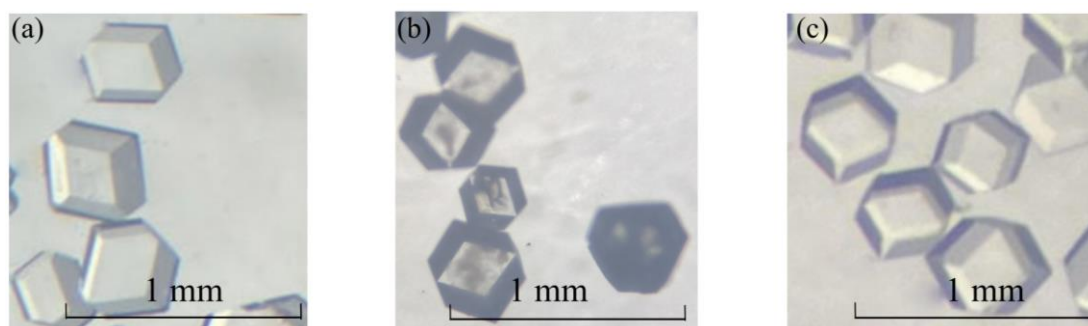
Fig. S12 The variation of single crystals under different conditions (a) as-synthesized, and (b) activated samples of MAF-7Br, and (c) activated MAF-7Br samples soaked in Bz.
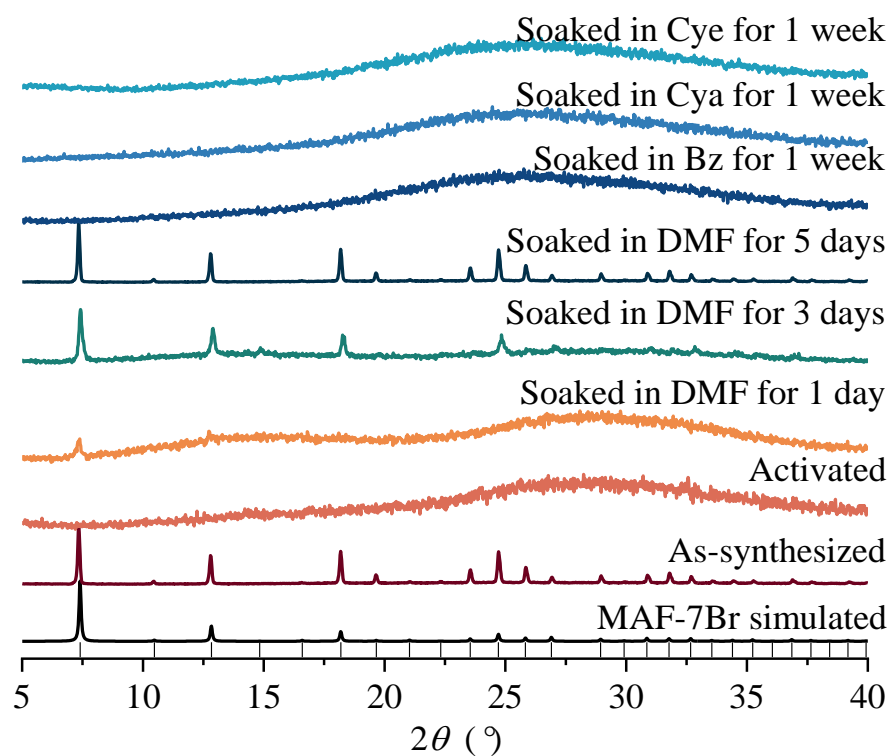
Fig. S13 PXRD patterns of MAF-7Br in different solvents at 298 K.
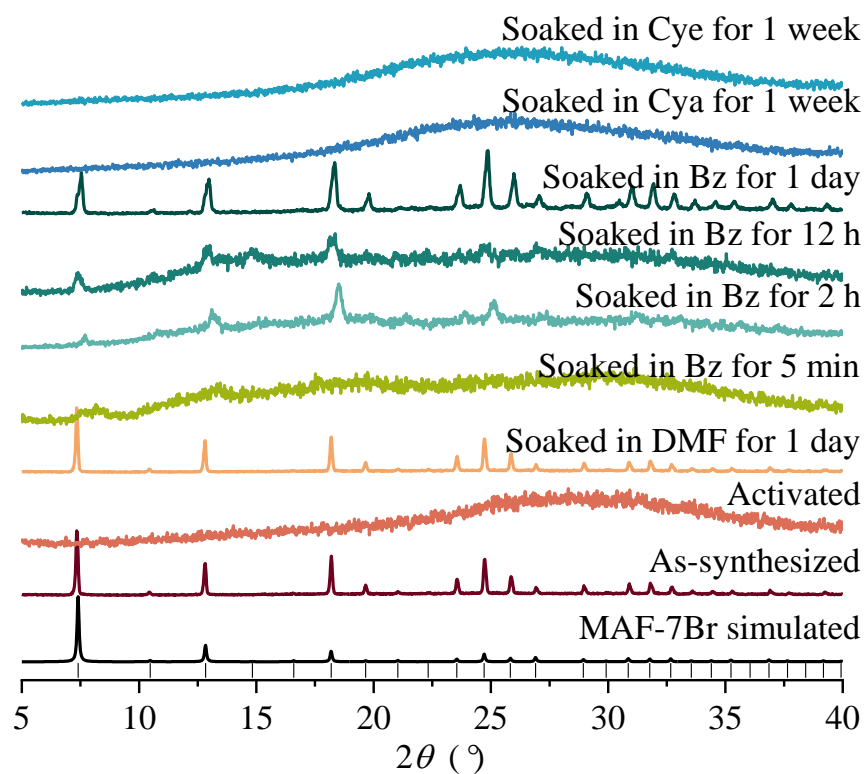
Fig. S14 PXRD patterns of MAF-7Br in different solvents at 313 K.
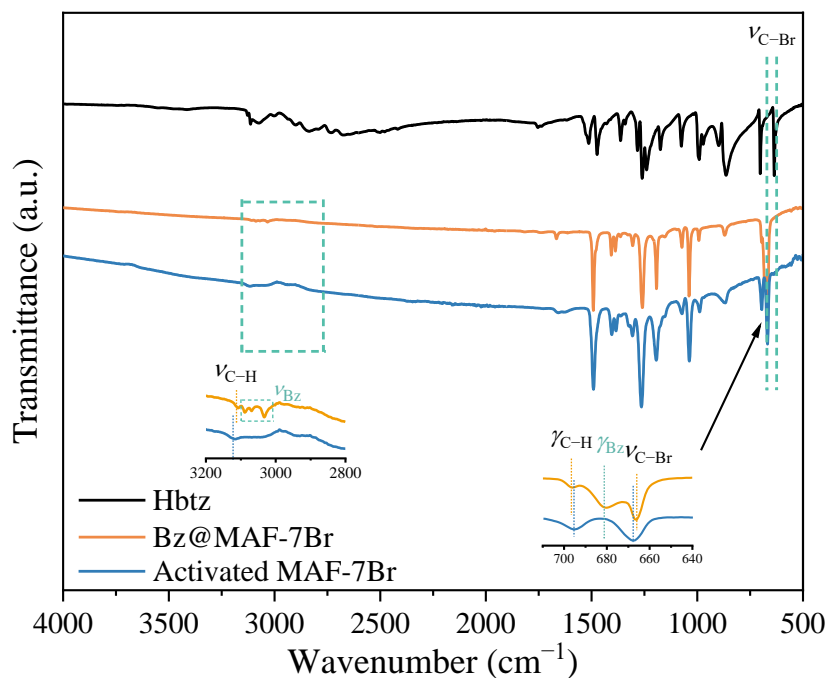
Fig. S15 ATR−FTIR spectra of Hbtz, activated MAF-7Br and Bz@MAF-7Br. Inset: Enlarged part for better comparison of $\nu_{C\text{-}H}$ and $\nu_{C\text{–}Br}$ in activated MAF-7Br and Bz@MAF-7Br.
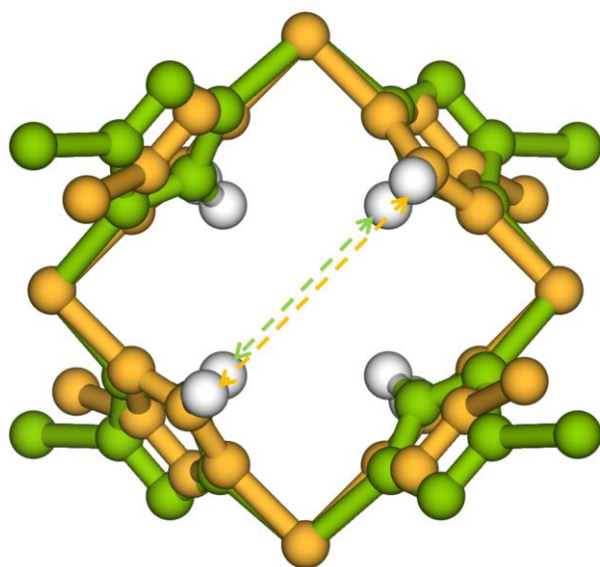
Fig. S16 Illustration of ligand rotation in the 4MR aperture. Green dashed arrow: The distance between the two nearest hydrogen atoms in Bz@MAF-7Br; Yellow dashed arrow: The distance between the two nearest hydrogen atoms if ligand rotation (when guest removal).
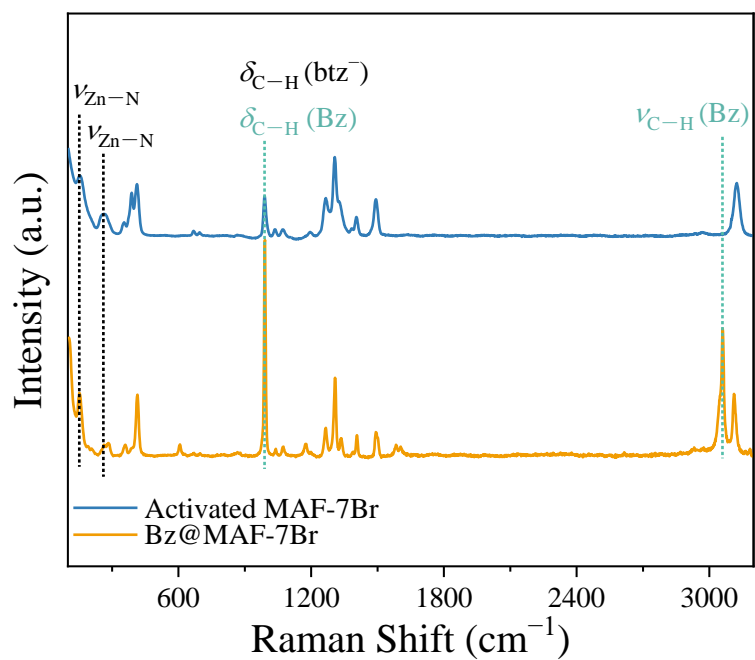
Fig. S17 Raman spectra of activated MAF-7Br and Bz@MAF-7Br.
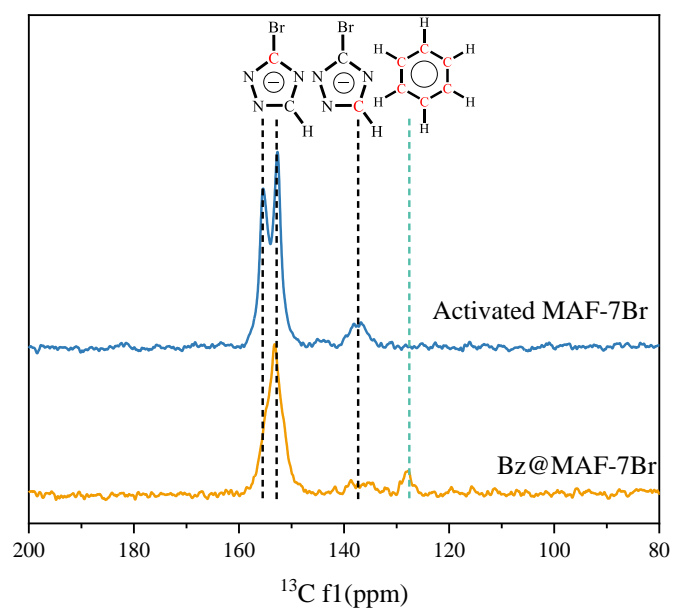
Fig. S18 Typical ^{13}C NMR spectrum of activated MAF-7Br and Bz@MAF-7Br.
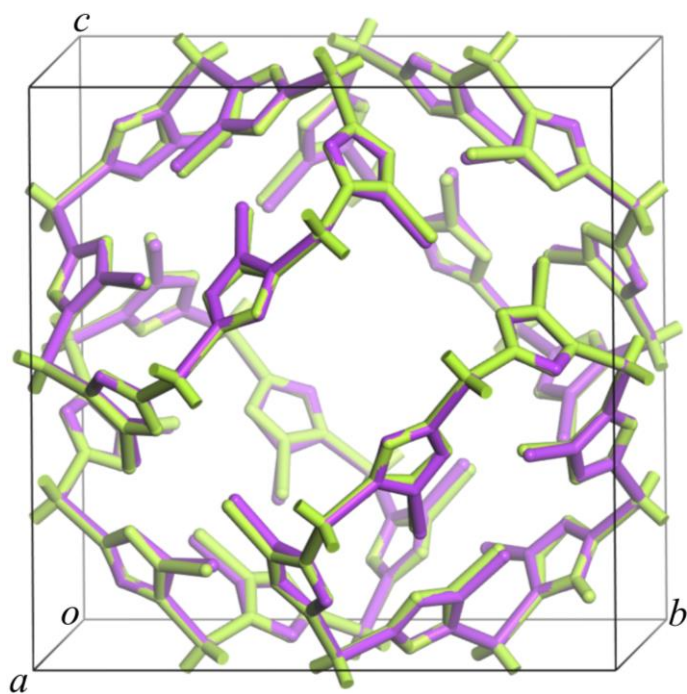
Fig. S19 The overlapped 3D frameworks of Bz@MAF-7Br (green) and MAF-7Br (purple). For clarity, the hydrogen atoms are omitted.
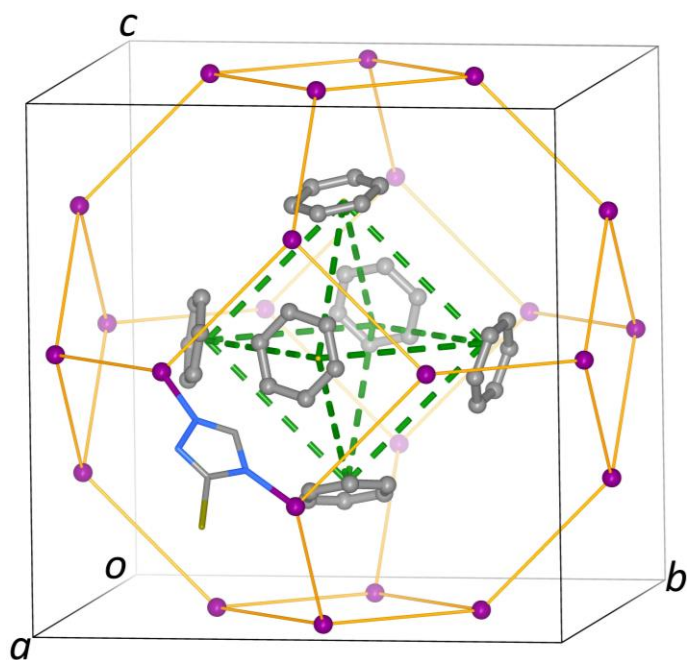
Fig. S20 The supramolecular hexamer of benzene molecules in the cavity of Bz@MAF-7Br. For clarity, the simplified framework retains Zn(II) nodes and only one btz⁻, and all hydrogen atoms on benzene are omitted.
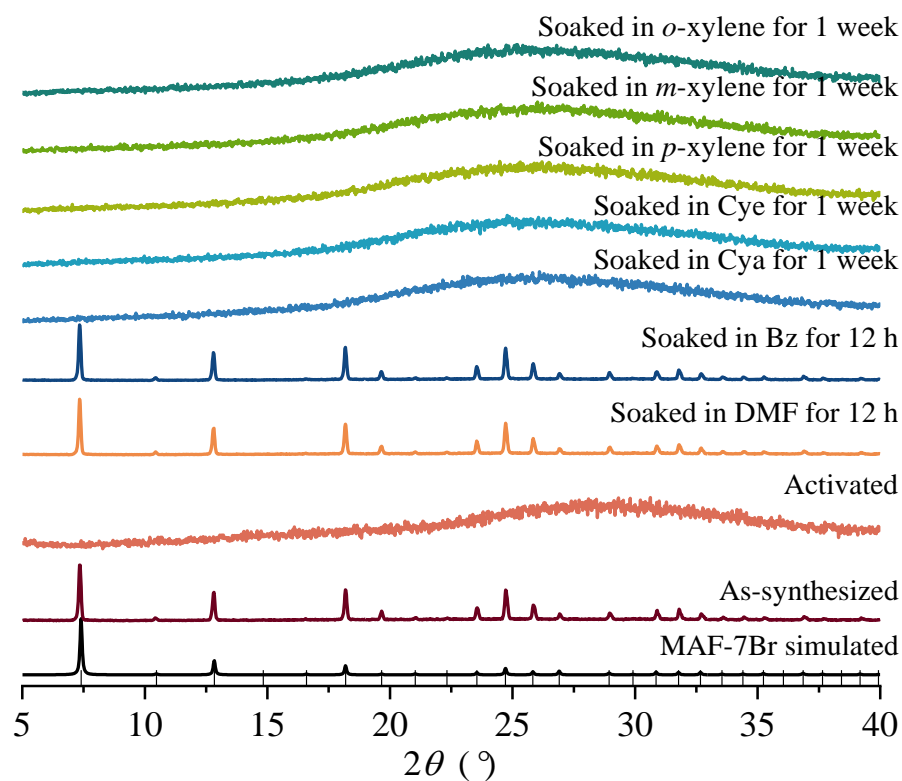
Fig. S21 PXRD patterns of MAF-7Br in different boiling solvents.
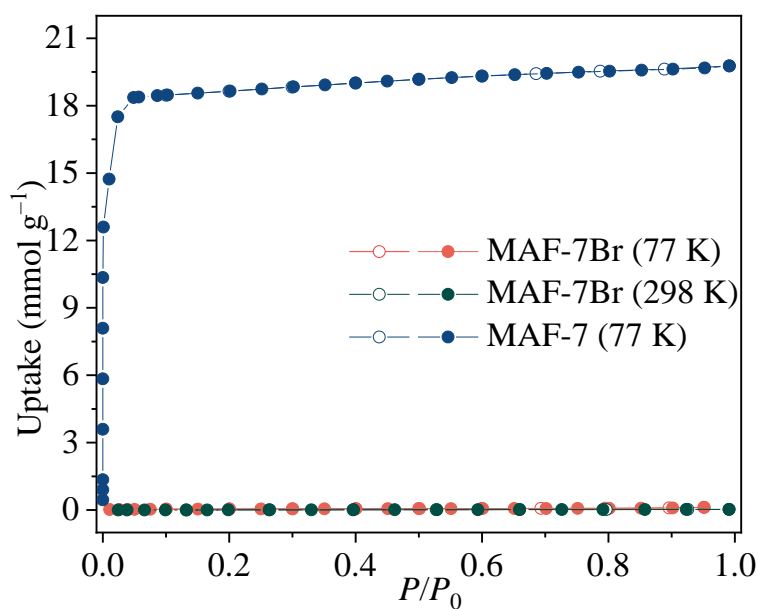
Fig. S22 Adsorption (solid) and desorption (open) isotherms of N_2 for MAF-7Br and MAF-7 at different temperatures.
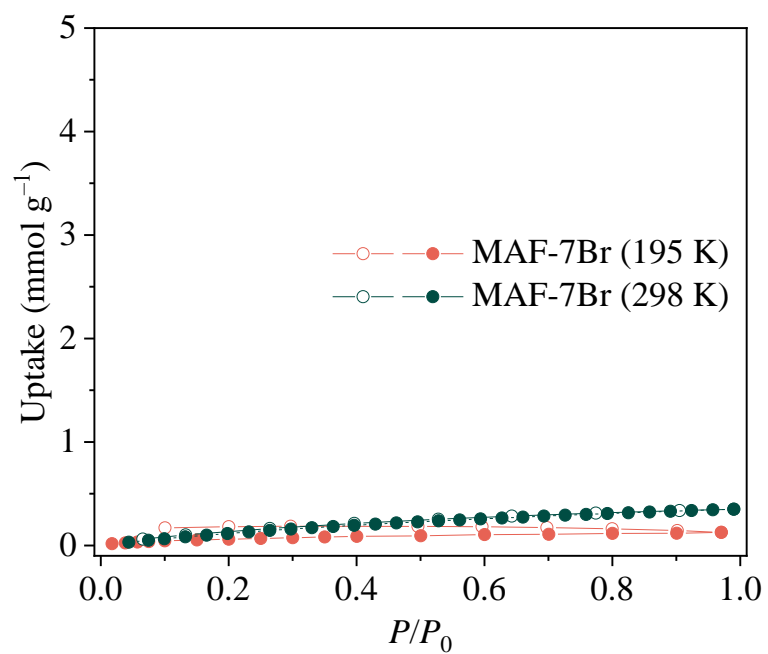
Fig. S23 Adsorption (solid) and desorption (open) isotherms of CO_2 for MAF-7Br at different temperatures.
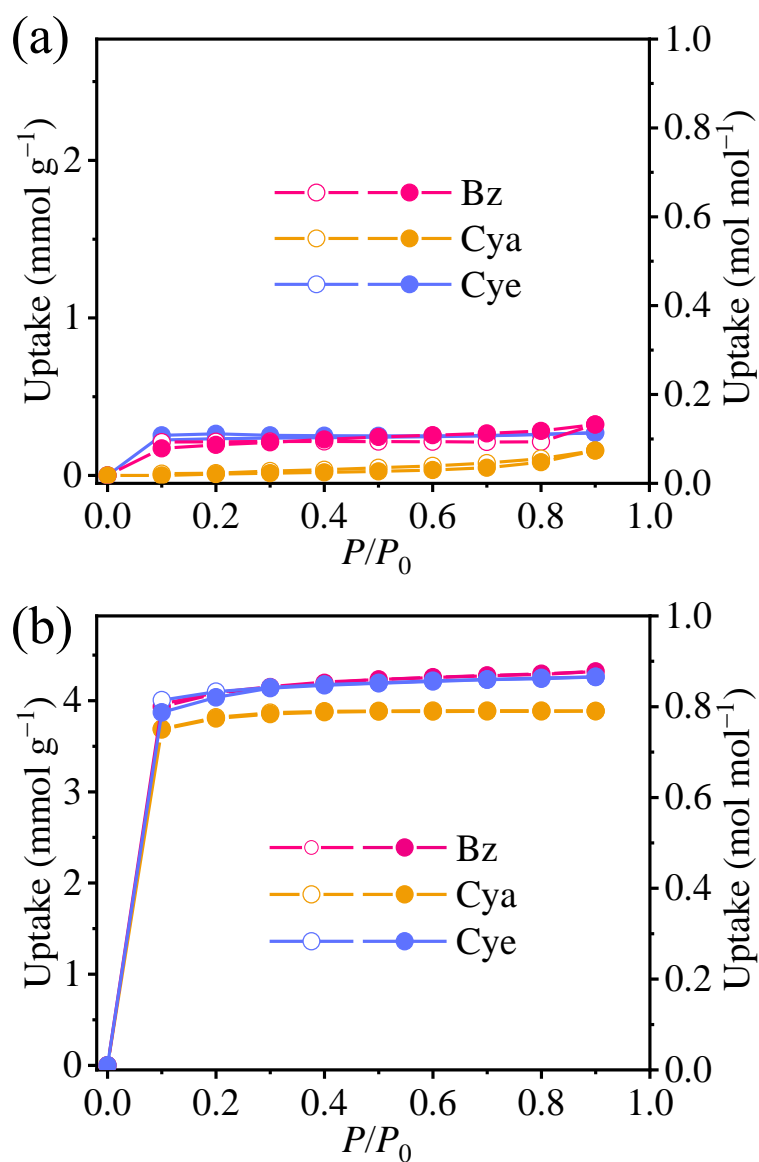
Fig. S24 Adsorption (solid) and desorption (open) isotherms of Bz/Cye/Cya for (a) MAF-7Br (b) MAF-7 at 298 K.
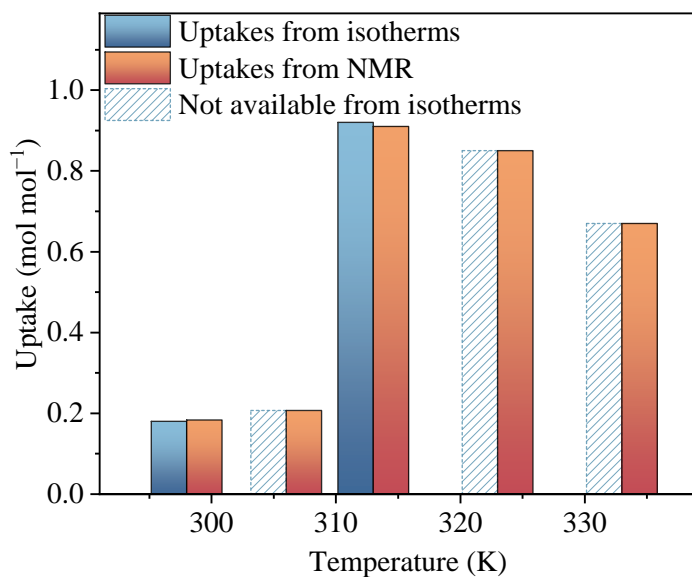
Fig. S25 Adsorption uptakes of Bz on MAF-7Br at different temperatures obtained from sorption isotherms and NMR analyses.
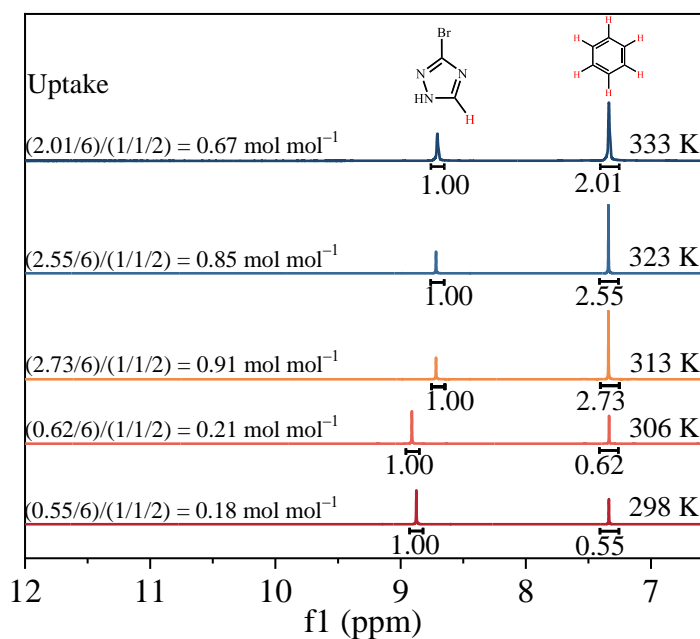
Fig. S26 Typical ^{1}H NMR spectrum of acid-digested MAF-7Br after being fully exposed to Bz vapor at different temperatures (the peaks shifted due to different acidification degree of samples).
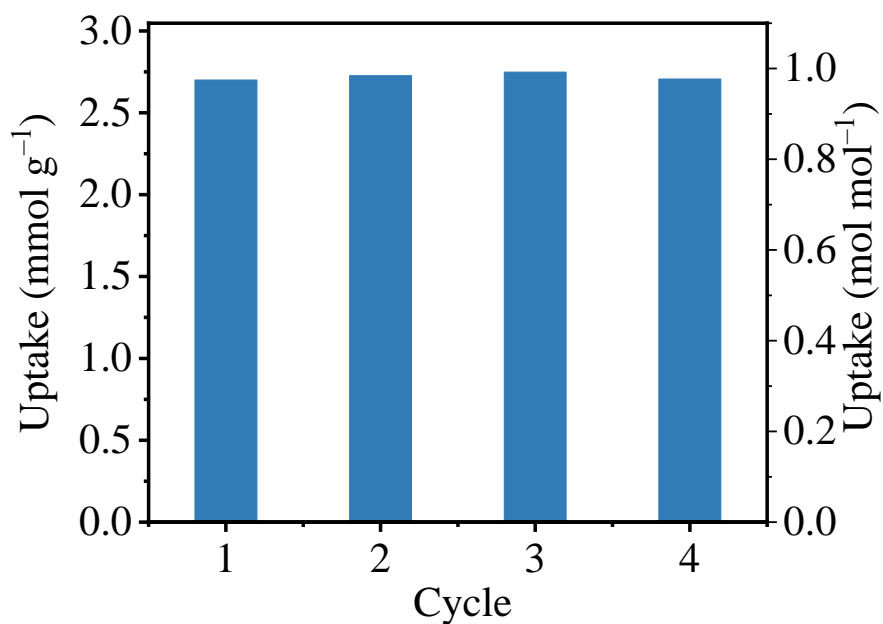
Fig. S27 Adsorption-desorption cycling stability of MAF-7Br in pure Bz at 313 K. The uptake was calculated by ^{1}H NMR.
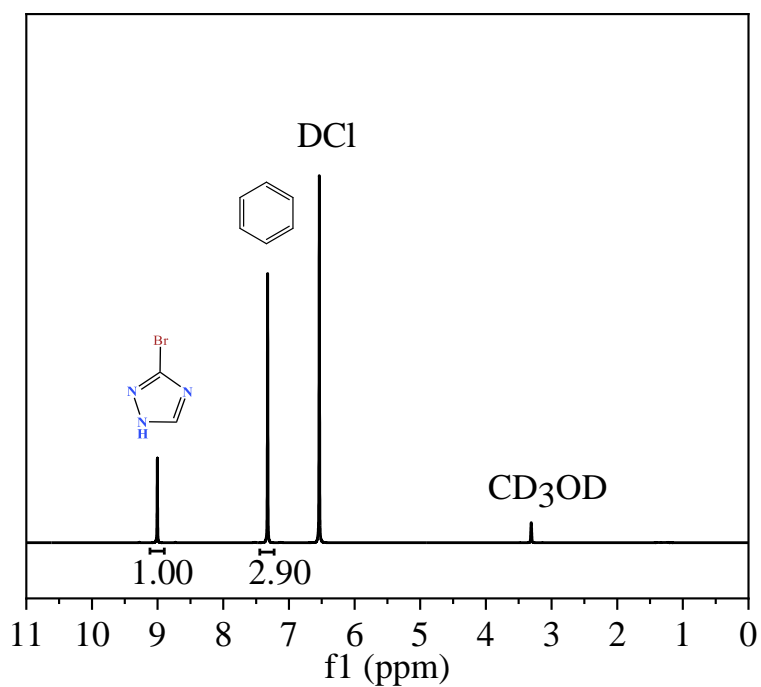
Fig. S28 Typical ^{1}H NMR spectrum of MAF-7Br after 4th adsorption in pure Bz. The calculated uptake for Bz is $(2.90/6)/(1/1/2) = 0.97$ mol mol^{-1}.
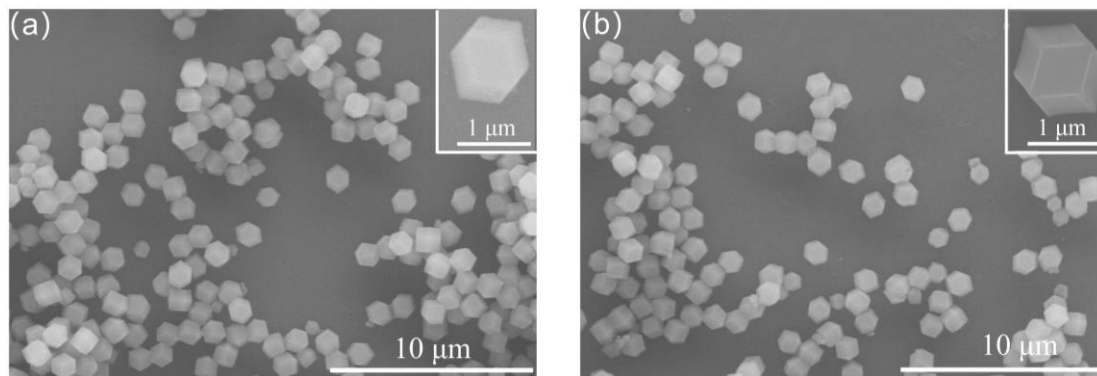
Fig. S29 SEM images of MAF-7Br after 4 adsorption-desorption cycles in (a) pure Bz and (b) Bz/Cya/Cye mixtures.

After 4th adsorption with Bz/Cya/Cye mixtures

After 4th adsorption with pure Bz

As-synthesized

MAF-7Br Simulated

2θ (°)
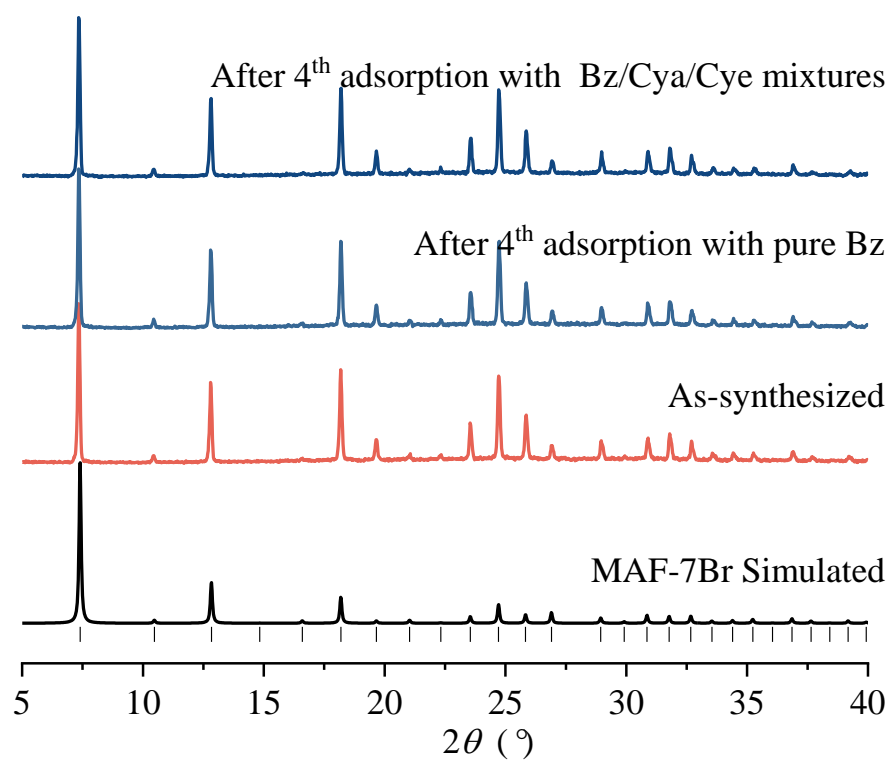
Fig. S30 PXRD patterns of MAF-7Br after the 4th adsorption-desorption cycle in pure Bz or Bz/Cya/Cye mixtures.
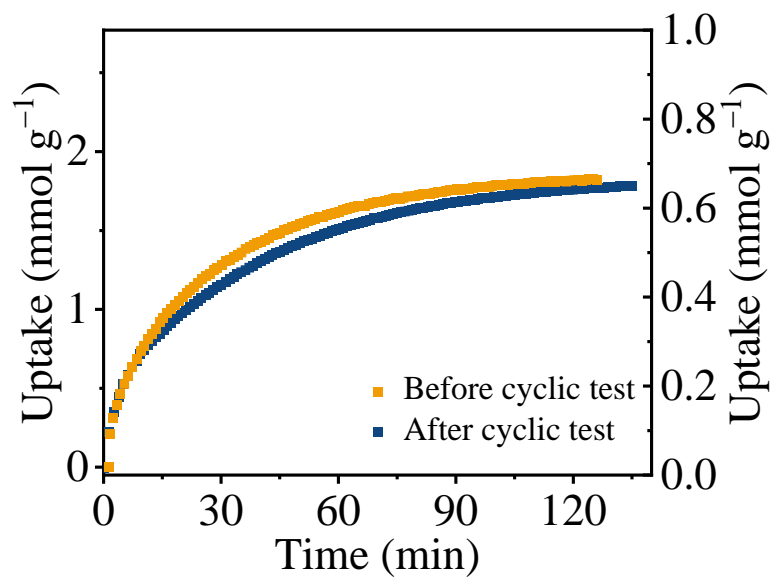
Fig. S31 Adsorption kinetic of Bz for MAF-7Br at $P/P_0 = 0.1$ before and after cyclic test.
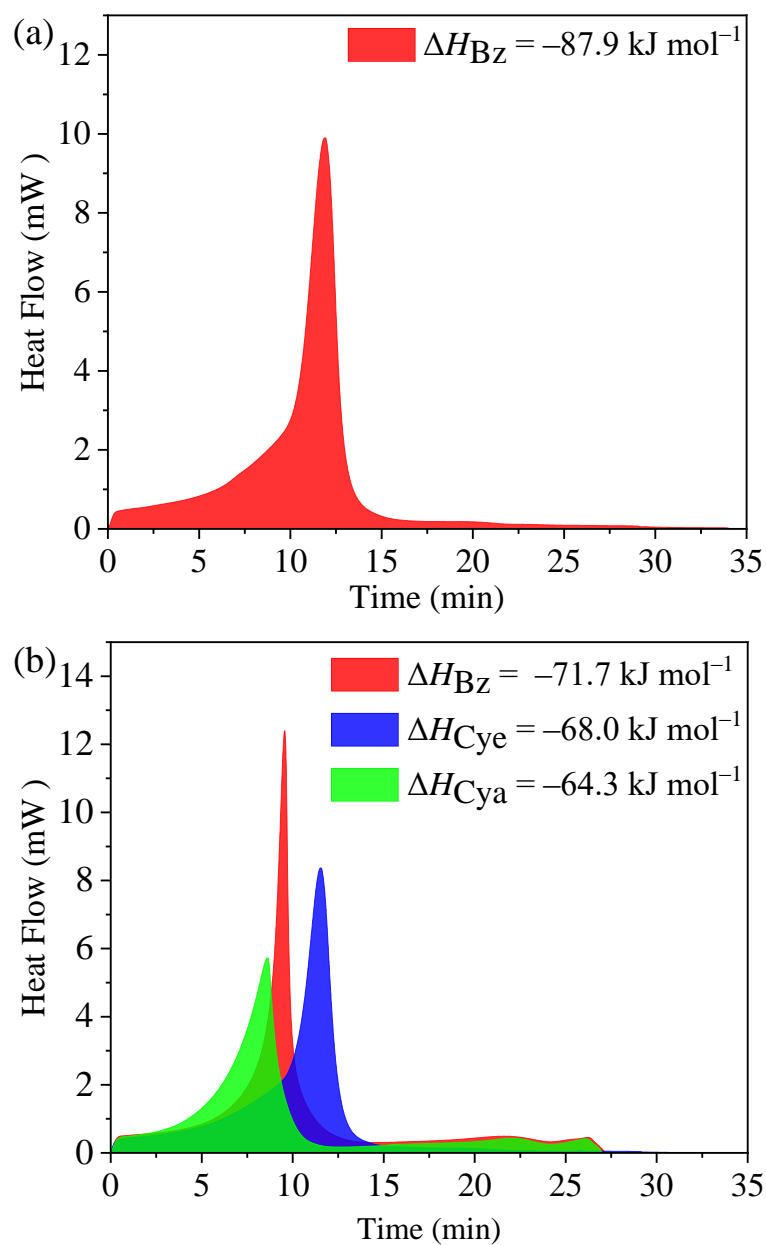
Fig. S32 Heat flows and ΔH values for the adsorption of C_6 cyclic hydrocarbons on (a) MAF-7Br and (b) MAF-7 obtained from DSC measurements. Considering that MAF-7Br barely adsorbs Cye and Cya, their data were not provided.
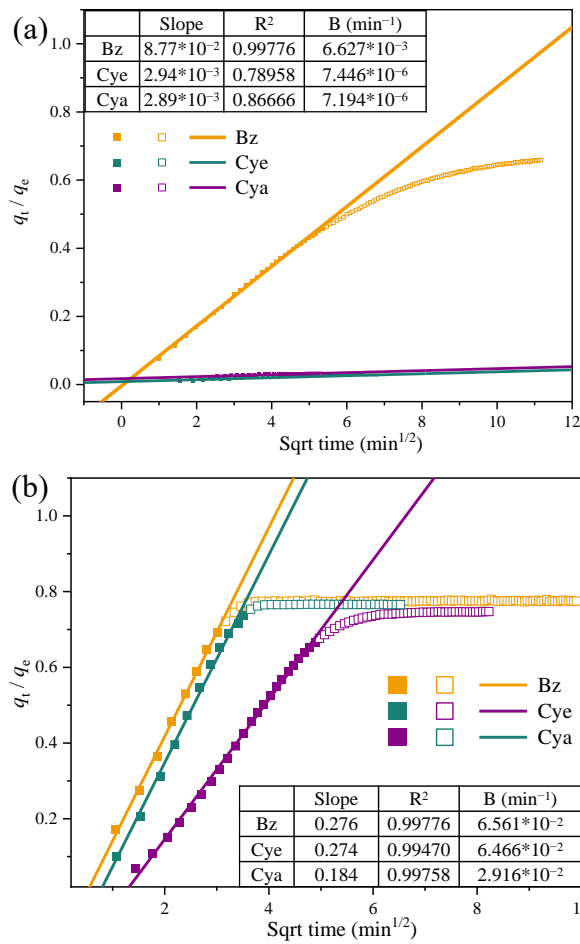
Fig. S33 Fitting curves of.single-component adsorption kinetics for Bz/Cye/Cya of (a) MAF-7Br and (b) MAF-7 at 313K.

(a)

Equation	y = a + b*x
Weight	No Weighting
Intercept	-0.00738 ±0.01036
Slope	1.82701E-7 ±7.30894E-10
Residual Sum of Squa	1.15654E-4
Pearson's r	0.99999
R-Square (COD)	0.99998
Adj. R-Square	0.99997

(b)

Equation	y = a + b*x
Weight	No Weighting
Intercept	4.40764E-4 ±2.397
Slope	1.71018E-7 ±1.406
Residual Sum of Squa	8.94129E-8
Pearson's r	0.99997
R-Square (COD)	0.99993
Adj. R-Square	0.99986

(c)

Equation	y = a + b*x
Weight	No Weighting
Intercept	5.60311E-4 ±4.57584E-
Slope	1.64191E-7 ±2.58453E-
Residual Sum of Squa	3.27646E-7
Pearson's r	0.99988
R-Square (COD)	0.99975
Adj. R-Square	0.9995

Fig. S34 The relationship between peak area and concentration of (a) Bz, (b) Cye and (c) Cya for GC.
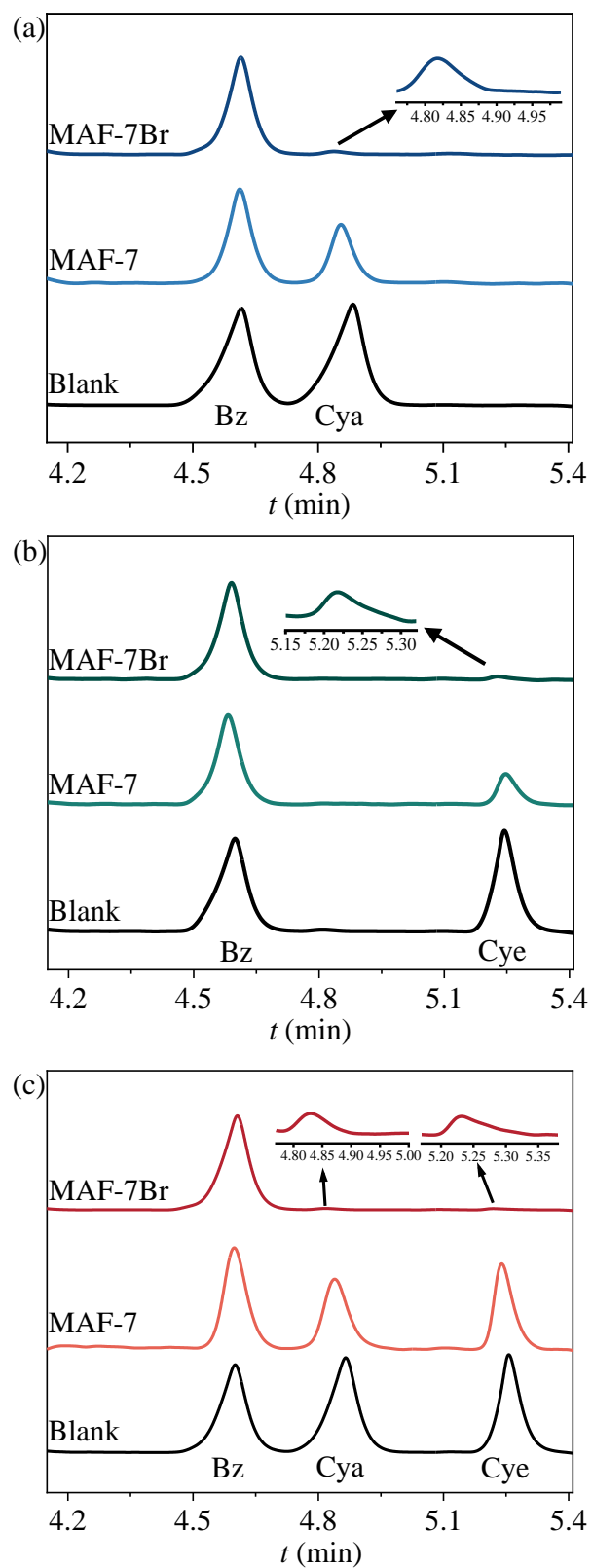
Fig. S35 Typical gas chromatography (GC) traces of the digestion solutions of MAF-7Br and MAF-7 after soaking in equimolar mixtures of (a) Bz/Cya, (b) Bz/Cye, and (c) Bz/Cya/Cye.
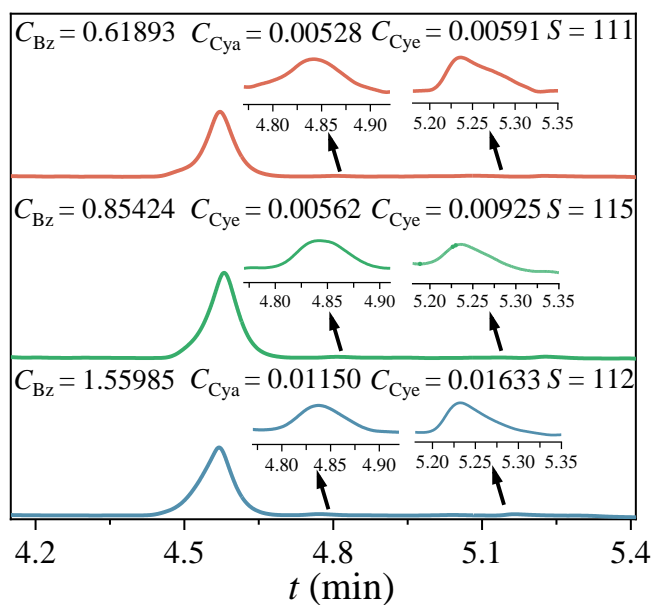
Fig. S36 Typical gas chromatography (GC) traces of the digestion solutions of MAF-7Br after soaking in equimolar mixtures of Bz/Cya/Cye in three batches. The concentration (C, mol L^{-1}) was obtained through standard curves on GC.
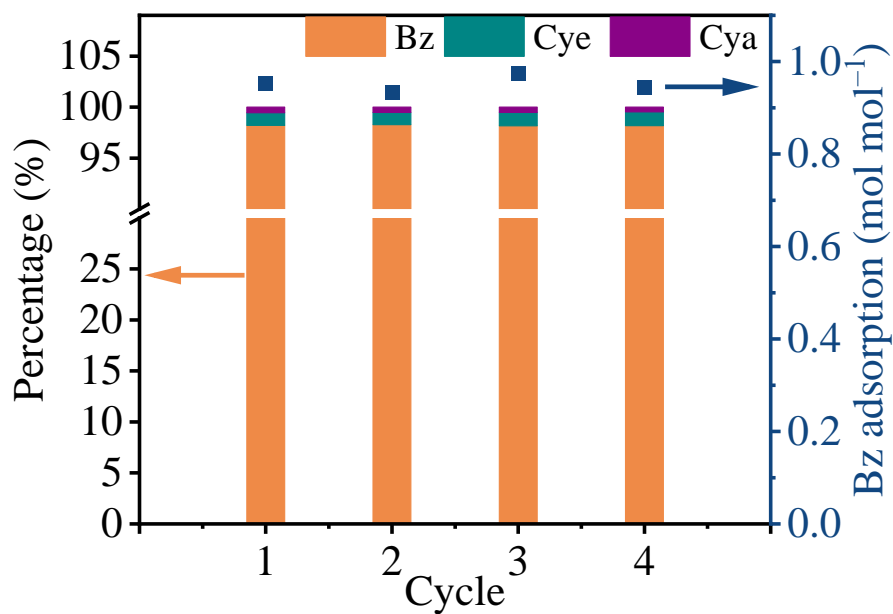
Fig. S37 Cycling stability of MAF-7Br in equimolar Bz/Cye/Cya mixtures.
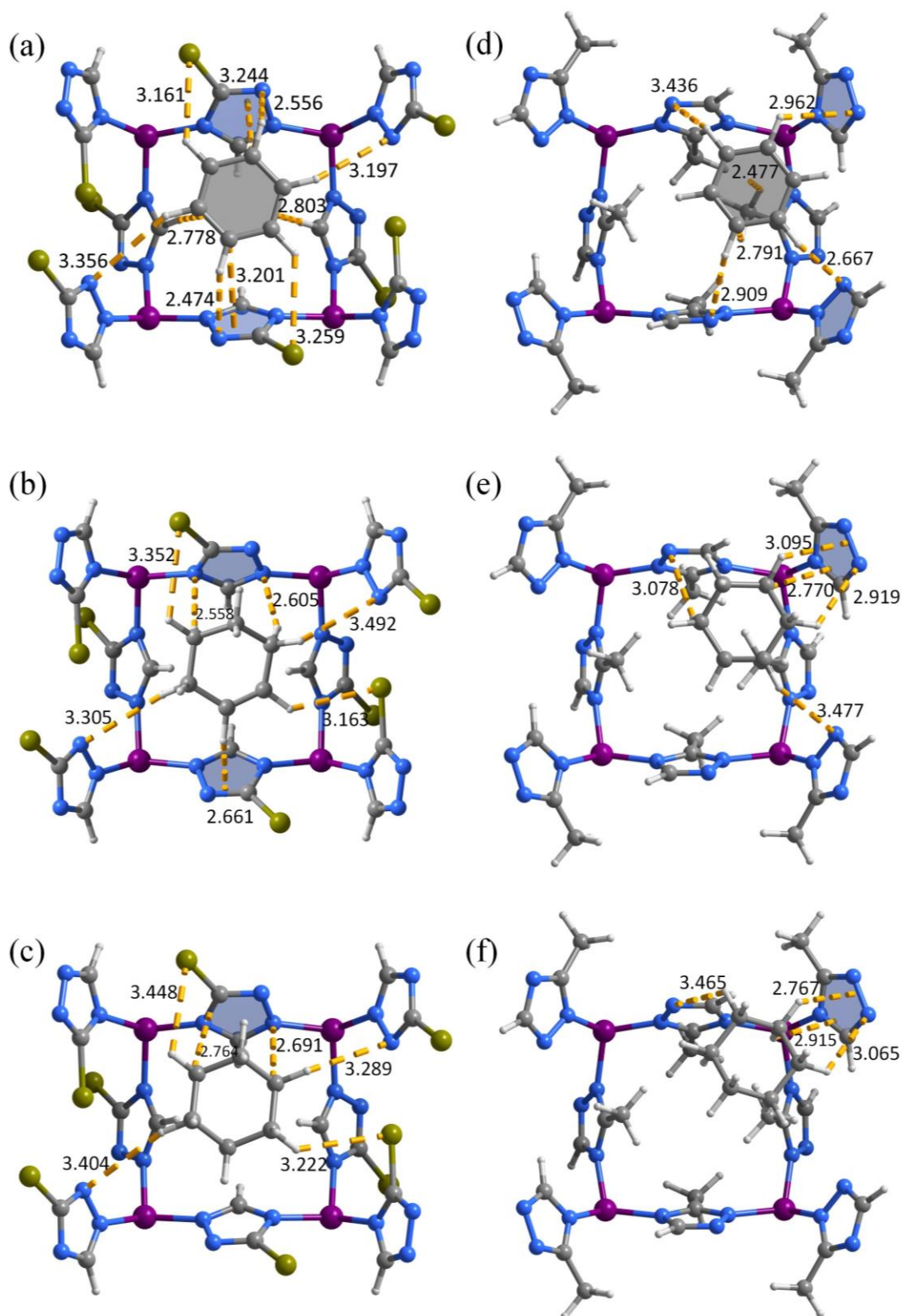
Fig. S38 The preferential adsorption sites of Bz/Cye/Cya in MAF-7Br and MAF-7 obtained by GCMC-PDFT simulations. (a-c) Host-guest structures between MAF-7Br and Bz (a), Cye (b), and Cya (c). (d-f) Host-guest structures between MAF-7 and Bz (d), Cye (e), and Cya (f). The prominent host-guest interactions represented in yellow dashed lines (distances in unit Å).
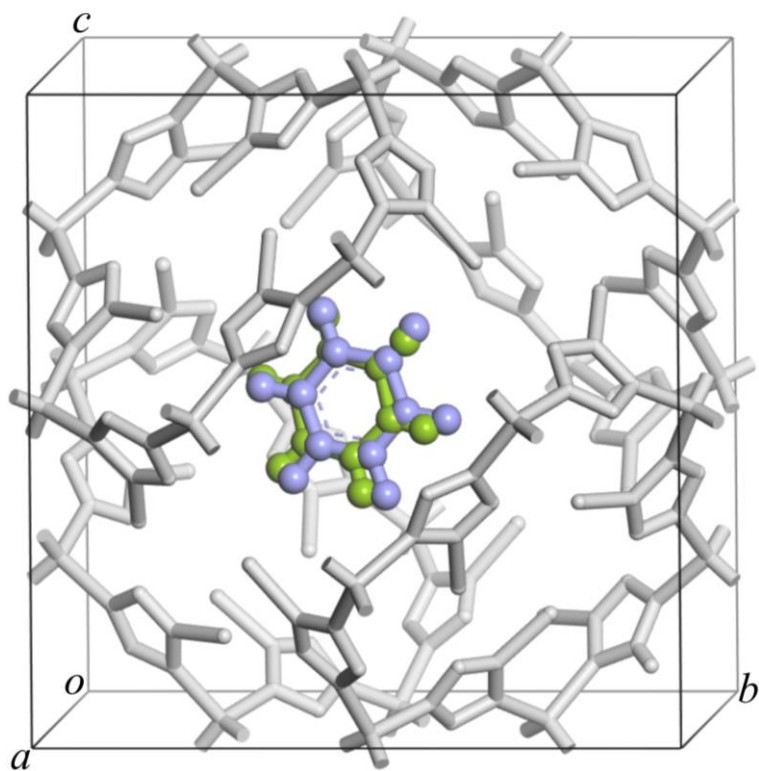
Fig. S39 The overlapped positions of Bz molecule from SCXRD (green) and GCMC simulations (lilac) of MAF-7Br. For clarity, the hydrogen atoms on the framework are omitted.

(a)

Equation	y = a + b*x
Intercept	-0.37519 ± 0.00676
Slope	1.1072E-4 ± 1.1723E-4
Residual Sum of Squares	11.33868
Pearson's r	0.28671
R-Square (COD)	0.0822
Adj. R-Square	0.08128

(b)

Equation	y = a + b*x
Intercept	0.2029 ± 0.00731
Slope	8.6542E-4 ± 1.5821E-4
Residual Sum of Squares	8.5226
Pearson's r	0.1901
R-Square (COD)	0.03614
Adj. R-Square	0.03493

(c)

Equation	y = a + b*x
Intercept	0.58987 ± 0.00593
Slope	8.1649E-5 ± 1.0852E-5
Residual Sum of Squares	7.81031
Pearson's r	0.23797
R-Square (COD)	0.05663
Adj. R-Square	0.05563

(d)

Equation	y = a + b*x
Intercept	1.12231 ± 0.04107
Slope	2.5642E-4 ± 7.1361E-5
Residual Sum of Squares	416.77451
Pearson's r	0.11342
R-Square (COD)	0.01282
Adj. R-Square	0.01183

(e)

Equation	y = a + b*x
Intercept	0.1923 ± 0.00647
Slope	1.4692E-4 ± 1.3988E-5
Residual Sum of Squares	6.66206
Pearson's r	0.3485
R-Square (COD)	0.12145
Adj. R-Square	0.12035

(f)

Equation	y = a + b*x
Intercept	0.50762 ± 0.02701
Slope	2.8176E-4 ± 4.8314E-5
Residual Sum of Squares	171.28572
Pearson's r	0.18481
R-Square (COD)	0.03415
Adj. R-Square	0.03316

Fig. S40 When the host was set rigid, linear fitting of MD-derived self-diffusion rates of (a) Bz, (b) Cye and (c) Cya for MAF-7Br, and (d) Bz (e) Cye and (f) Cya for MAF-7.
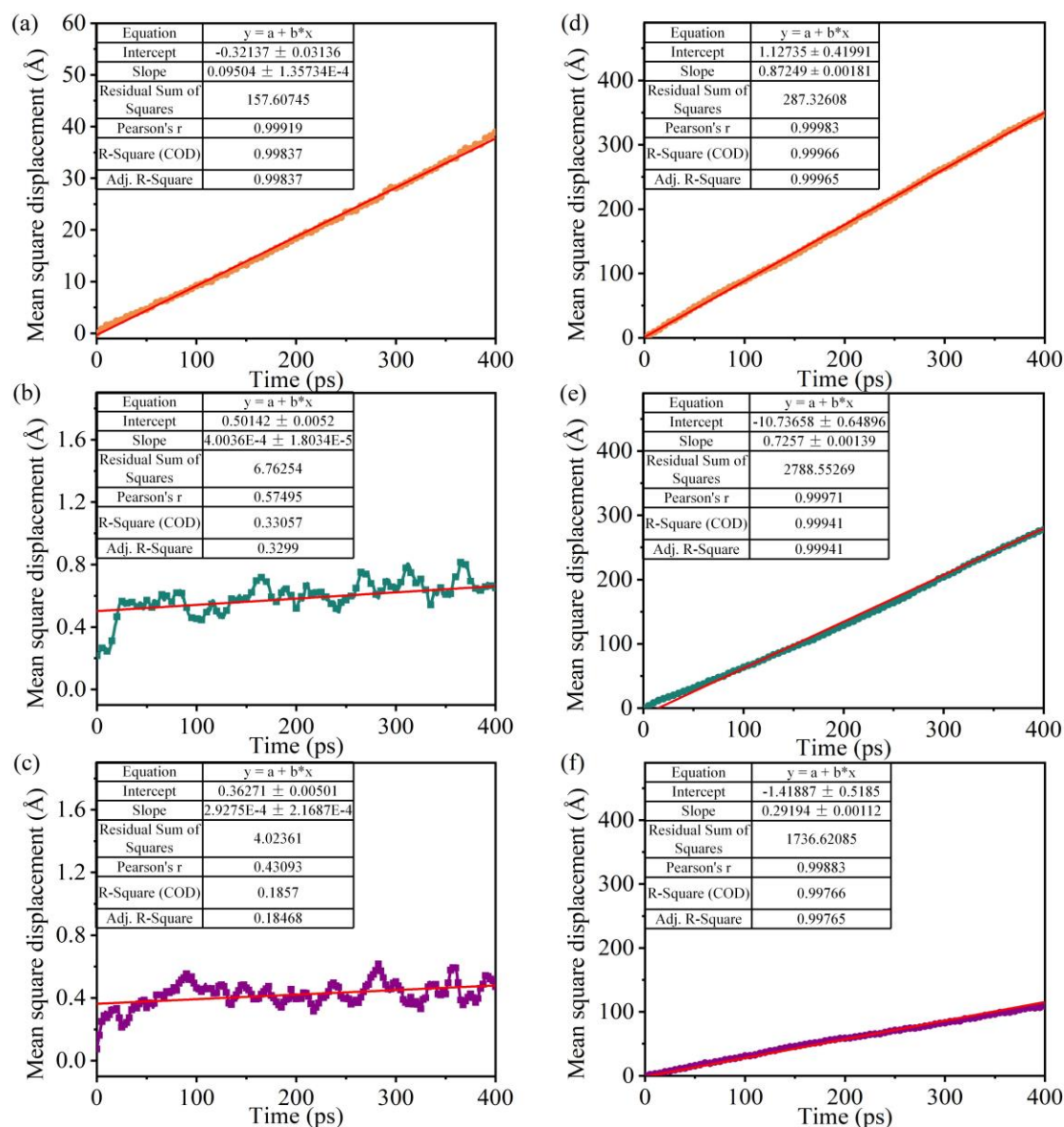
Fig. S41 When the host was set flexible, linear fitting of MD-derived self-diffusion rates of (a) Bz, (b) Cye and (c) Cya for MAF-7Br, and (d) Bz (e) Cye and (f) Cya for MAF-7.
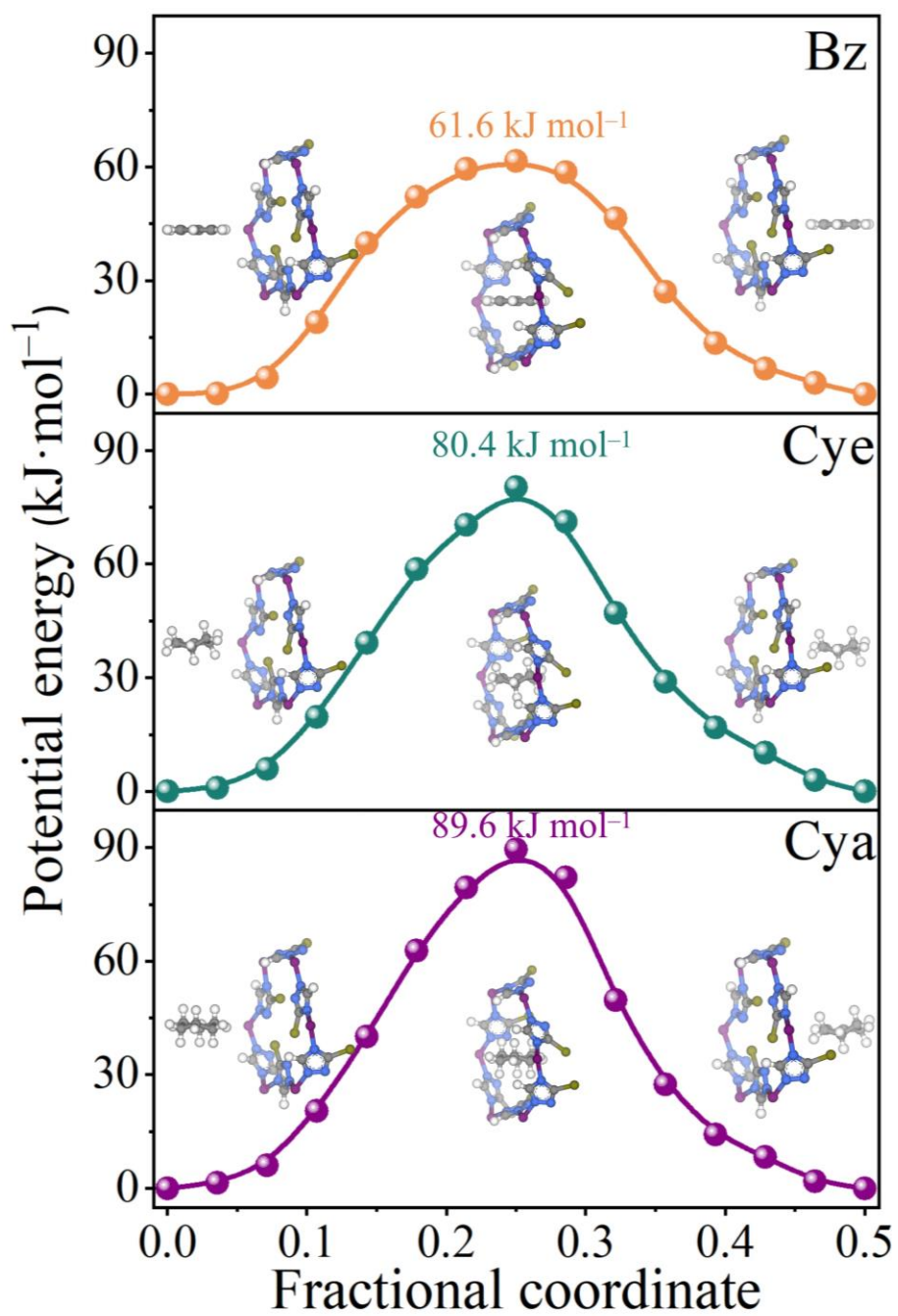
Fig. S42 The gating energy barriers for Bz (up), Cye (middle) and Cya (down) in MAF-7Br. The insets show the snapshots of Bz/Cye/Cya diffusion processes at the 6MR aperture.
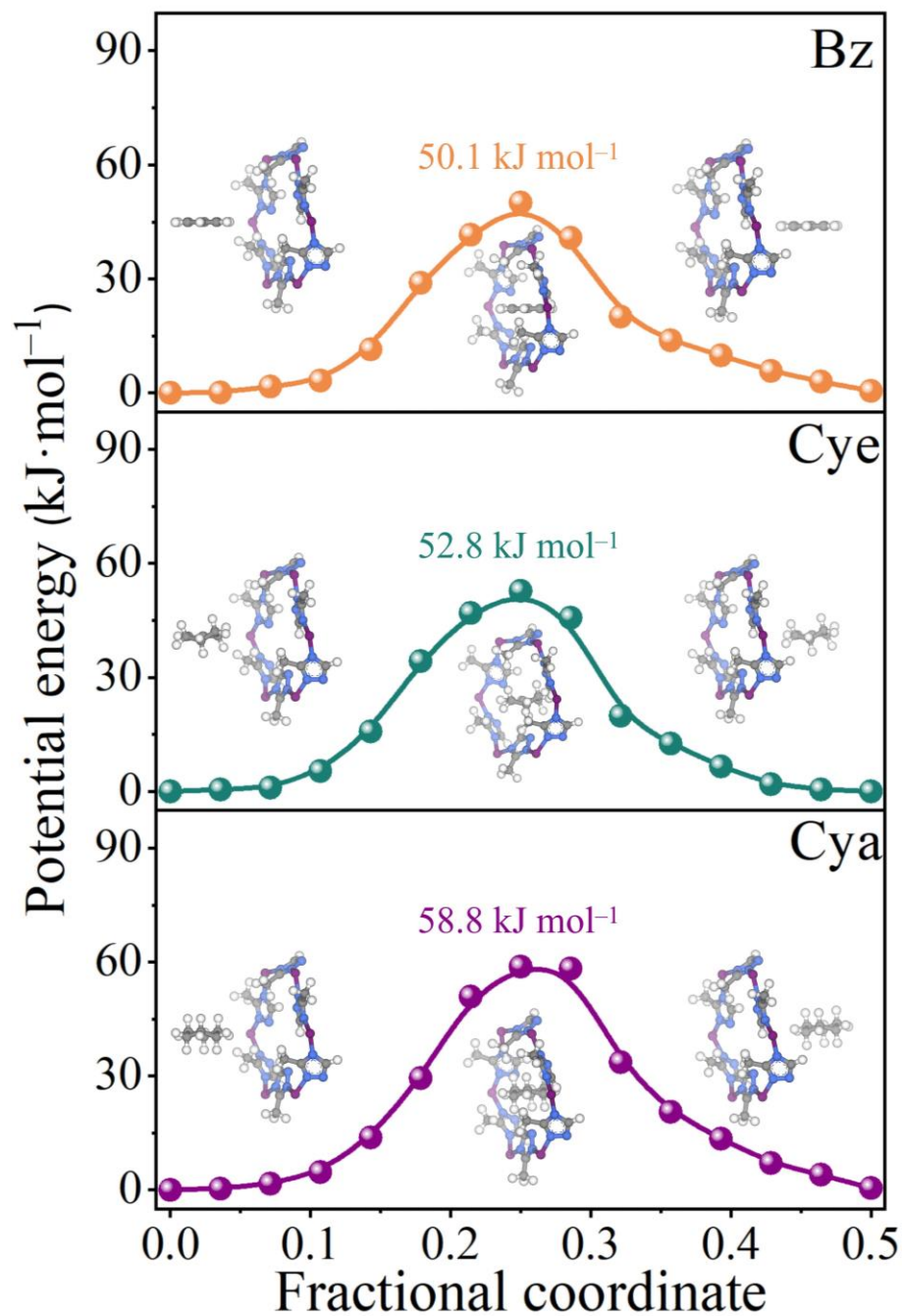
Fig. S43 The gating energy barriers for Bz (up), Cye (middle) and Cya (down) in MAF-7. The insets show the snapshots of Bz/Cye/Cya diffusion processes at the 6MR aperture.
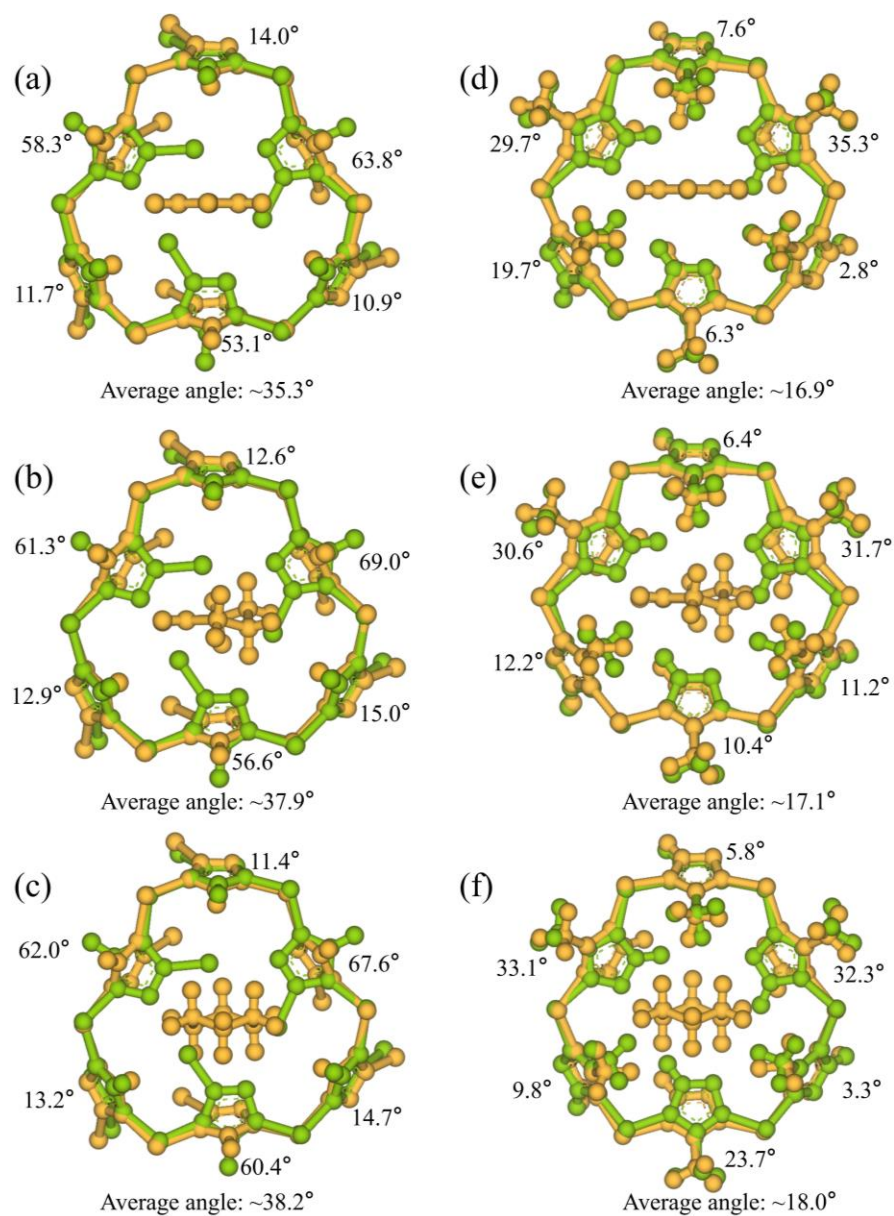
Fig. S44 The maximum rotation angles of triazolate ring in (a-c) MAF-7Br and (e-f) MAF-7 during the PDFT simulated Bz (a,d), Cye (b,e), and Cya (c,f) diffusion. To differentiate between the various structural states, green indicates the closed gate states, while yellow represents the states at maximum gate rotation angles. The average value of six rotation angles were shown under the corresponding figures.
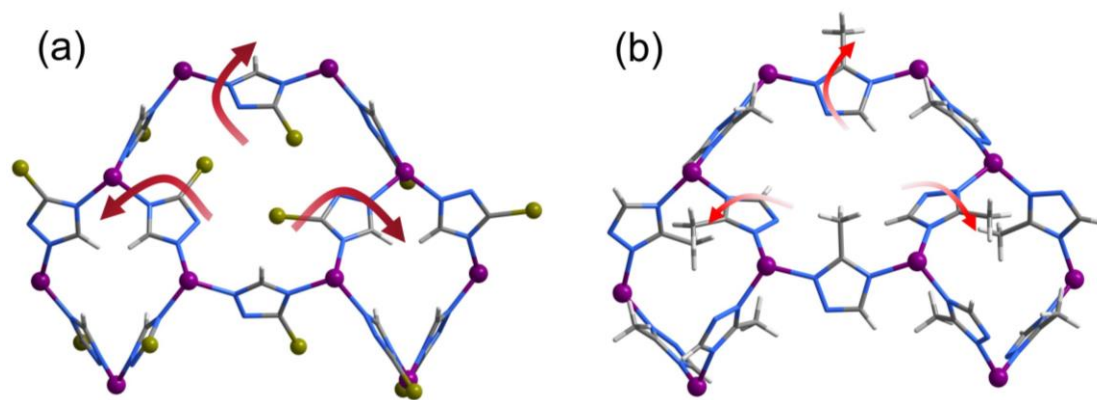
Fig. S45 The rotation degree of triazolate ring in (a) MAF-7Br and (b) MAF-7, the thicker and longer red arrows in MAF-7Br illustrate that triazolate rings is more difficult to rotate, but it has a larger rotation range if it could rotate.
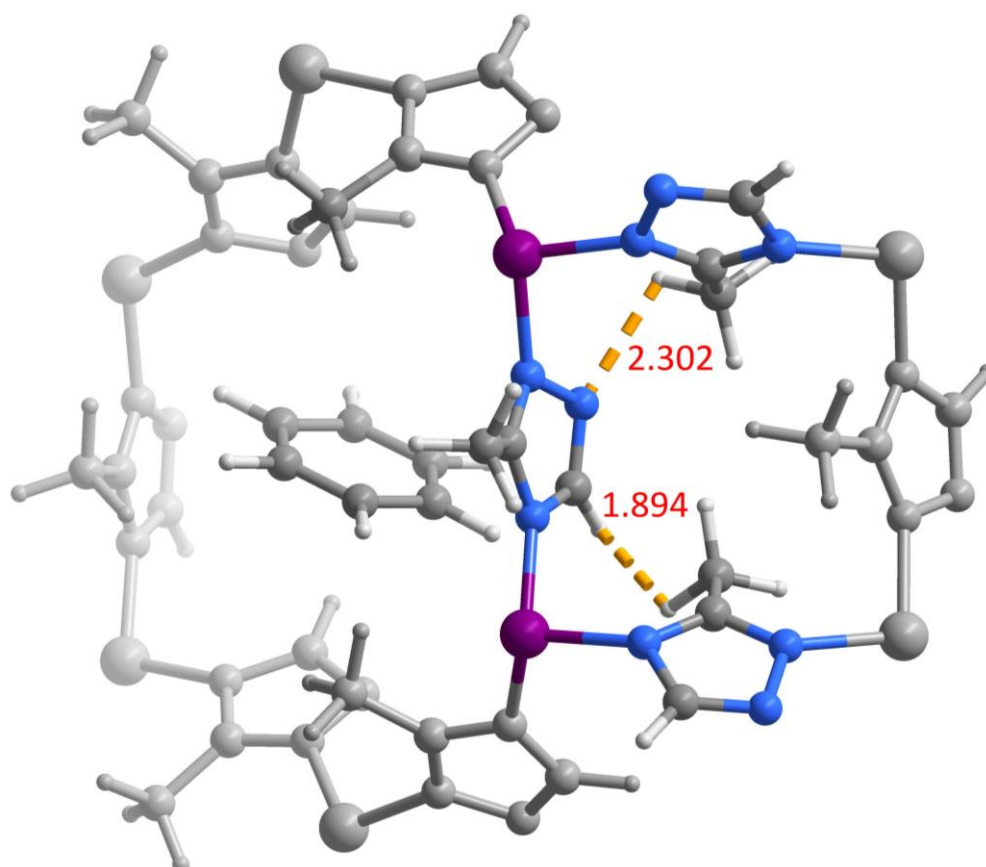
Fig. S46 The structure of MAF-7 matching swing angle with MAF-7Br obtained by GCMC-PDFT simulations. The atoms that are too close are represented in yellow dashed lines (distances in unit Å).

Table S1. Crystal data and structure refinement results.

Complex	MAF-7Br	Bz@MAF-7Br
Formula	$C_7H_9Br_2N_7OZn$	$C_{10}H_8Br_2N_6Zn$
Formula weight	432.40	437.41
Temperature (K)	100.00(10)	100.00(10)
Crystal system	cubic	cubic
Space group	$I\bar{4}3m$	$I\bar{4}3m$
a / Å	16.77164(5)	16.77190(10)
b / Å	16.77164(5)	16.77190(10)
c / Å	16.77164(5)	16.77190(10)
α / °	90	90
β / °	90	90
γ / °	90	90
V / Å^3	4717.66(4)	4717.88(8)
Z	12	12
D_c / g cm^{-3}	1.826	1.847
reflns coll.	33076	29166
unique reflns	843	969
R_{int}	0.0339	0.0525
$R_1 [I > 2\sigma(I)]^a$	0.0857	0.0468
$wR_2 [I > 2\sigma(I)]^b$	0.2615	0.1295
R_1 (all data)	0.0857	0.0468
wR_2 (all data)	0.2616	0.1295
GOF	1.093	1.087
Flack	-0.007(12)	0.03(10)
Largest diff. peak / e Å^{-3}	1.65	1.28
Largest diff. hole / e Å^{-3}	-1.3	-0.55

[a] $R_1 = \sum||F_o|-|F_c||/\sum|F_o|$;

[b] $wR_2 = [\sum w(F_o^2 - F_c^2)^2/\sum w(F_o^2)^2]^{1/2}$

Table S2. Summary of benzene-cyclohexene-cyclohexane adsorption and separation performances of state-of-the-art adsorbents.

Materials	Uptake (mmol g^{-1})			Temp.	Selectivity[a]			Ref.
	Bz	Cye	Cya	(K)	Bz/Cya	Bz/Cye	Bz/Cye/Cya	
MAF-7Br	2.55	0.17	0.17	313	65.5	43.4	**113**	This work
MAF-7	3.88	3.88	3.75	313	2.2	1.7	1.4	
Mn-DHBQ	2.9	2.8	1.4	303	97.7	19.7	88.1	3
	2.7	2.0	0.08	333	120.1	**44.8**	104.5	
BNF-2	1.81	—	—	353	124.0[b]	44.5[b]	34.7[b]	11
Naphthotubes 1a	1.72	0	0	298	4.3[b]	2.3[b]	—	12
Naphthotubes 1b	2.17	1.43	0.46	298	17.5[b]	9.75[b]	9.20[b]	
MAF-67	1.73	1.67	1.34	298	2.5	1.6	—	13
UiO-66	2.7	—	2.0	298	3[b]	—	—	14
UiO-66-Cu^{II}	6.0	—	4.0	298	31[b]	—	—	
MFM-300(Sc)	5.0	—	3.0	298	**166[b]**	—	—	
MFM-300(Cr)	4.1	—	2.3	298	103[b]	—	—	
MFM-300(Fe)	3.9	—	2.3	298	75[b]	—	—	
MAF-stu-13	2.5	—	0.2	298	138	—	—	15
[Zn$_4$(EGO$_2$)$_2$(tdc)$_2$(dabco)]	0.95	—	0.09	298	77	—	—	16
[Zn$_4$(PrO$_2$)$_2$(tdc)$_2$(dabco)]	1.15	—	0.24	298	7	—	—	
ZnL'	1.51	—	0.24	298	20	—	—	17
TUS-88	5.94	—	2.66	298	2.46[c]	—	—	18
JUC-641	7.25	—	3.48	298	1.80[c]	—	—	19
JUC-642	7.45	—	3.41	298	1.91[c]	—	—	
CCTF-1	11.24	—	5.25	298	1.74[c]	—	—	20
CCTF-2	8.33	—	3.70	298	1.80[c]	—	—	
CCTF-3	1.75	—	0.73	298	1.90[c]	—	—	
4A	0.059	—	0.011	298	1.2[c]	—	—	21
NAY	2.09	—	1.71	298	2.3[c]	—	—	
SSZ-74-100	2.12	—	1.49	298	9.5[c]	—	—	
ZSM-5-F	1.82	—	0.479	298	26.4[c]	—	—	
E5 activated carbon	32.44	—	4.72	298	11.1[c]	—	—	22
QB activated carbon	40.32	—	13.68	298	4.73[c]	—	—	

[a]: Selectivity values are calculated from GC analysis.

[b]: Selectivity values are calculated from NMR analysis.

[c]: Selectivity values are calculated from column breakthrough experiment.

Table S3. Distances (Å) of host-guest supramolecular interactions in MAF-7Br and MAF-7 obtained from GCMC-PDFT calculations.

Host	Guest	Type	The shortest distance (Å)		
MAF-7Br	Bz	C–H$_{host}$···π_{guest}	2.474	2.556	
		C–H$_{guest}$···π_{host}	2.778	2.803	
		π_{guest}···π_{host}	3.201	3.244	
		C–H$_{guest}$···N$_{host}$	3.197	3.356	
		C–H$_{guest}$···Br$_{host}$	3.161	3.259	
	Cye	C–H$_{guest}$···π_{host}	2.558	2.605	2.661
		C–H$_{guest}$···N$_{host}$	3.305	3.492	
		C–H$_{guest}$···Br$_{host}$	3.163	3.352	
	Cya	C–H$_{guest}$···π_{host}	2.691	2.764	
		C–H$_{guest}$···N$_{host}$	3.289	3.404	
		C–H$_{guest}$···Br$_{host}$	3.222	3.448	
MAF-7	Bz	C–H$_{host}$···π_{guest}	2.477	2.791	
		C–H$_{guest}$···π_{host}	2.667	2.962	
		C–H$_{guest}$···N$_{host}$	2.909	3.436	
	Cye	C–H$_{guest}$···π_{host}	2.770	3.095	
		C–H$_{guest}$···N$_{host}$	2.919	3.078	3.477
	Cya	C–H$_{guest}$···π_{host}	2.787	2.915	
		C–H$_{guest}$···N$_{host}$	3.065	3.465	

Table S4. The diffusion rates (m^2·s^{-1}) of Bz/Cye/Cya for MAF-7Br and MAF-7 obtained from molecular dynamics (MD) simulations.

Diffusion rates	Bz	Cye	Cya
MAF-7Br (rigid)	1.8×10^{-13}	1.5×10^{-13}	1.4×10^{-13}
MAF-7 (rigid)	4.3×10^{-13}	2.4×10^{-13}	4.6×10^{-13}
MAF-7Br (flexible)	0.2×10^{-9}	5×10^{-13}	7×10^{-13}
MAF-7 (flexible)	1.4×10^{-9}	1.2×10^{-9}	0.5×10^{-9}

Table S5. Energy barriers (kJ mol^{-1}) for Bz/Cye/Cya in MAF-7Br with different substituent groups obtained from PDFT calculations.

Energy barriers	−Br	−H (hypothesis)	Difference
Bz	61.6	29.6	32.0
Cye	80.4	47.5	33.0
Cya	89.6	54.5	35.1
Average	/	/	33.4

References

1. L. Zhang, H.-W. Chen, P.-X. Liu, Y. Chen, Y.-T. Liu, R.-B. Lin, X.-M. Chen, J.-P. Li and L.-B. Li, *J. Colloid. Interface Sci.*, 2024, **656**, 538.
2. M.-Y. Zhou, X.-W. Zhang, H. Yi, Z.-S. Wang, D.-D. Zhou, R.-B. Lin, J.-P. Zhang and X.-M. Chen, *J. Am. Chem. Soc.*, 2024, **146**, 12969.
3. F. Xie, L.-H. Chen, E. M. C. Morales, S. Ullah, Y.-W. Fu, T. Thonhauser, K. Tan, Z.-B. Bao and J. Li, *Nat. Commun.*, 2024, **15**, 2240.
4. Z.-M. Ye, X.-F. Zhang, D.-X. Liu, Y.-T. Xu, C. Wang, K. Zheng, D.-D. Zhou, C.-T. He and J.-P. Zhang, *Sci. China Chem.*, 2022, **65**, 1552.
5. Z.-M. Ye, X.-W. Zhang, P.-Q. Liao, Y. Xie, Y.-T. Xu, X.-F. Zhang, C. Wang, D.-X. Liu, N.-Y. Huang, Z.-H. Qiu, D.-D. Zhou, C.-T. He and J.-P. Zhang, *Angew. Chem. Int. Ed.*, 2020, **59**, 23322.
6. Q.-L. Hu, S.-Y. Pang and D. Wang, *Sep. Purif. Rev.*, 2022, **51**, 281.
7. Z.-F. Jiang, W.-J. Xue, H.-L. Huang, H.-J. Zhu, Y.-X. Sun and C.-L. Zhong, *Chem. Eng. J.*, 2023, **454**, 140093.
8. J. P. Perdew, K. Burke and M. Ernzerhof, *Phys. Rev. Lett.*, 1996, **77**, 3865.
9. X.-W. Zhang, D.-D. Zhou and J.-P. Zhang, *Chem*, 2021, **7**, 1006.
10. D.-D. Zhou, P. Chen, C. Wang, S.-S. Wang, Y. Du, H. Yan, Z.-M. Ye, C.-T. He, R.-K. Huang, Z.-W. Mo, N.-Y. Huang and J.-P. Zhang, *Nat. Mater.*, 2019, **18**, 994.
11. C.-H. Liu, L.-J. Chen, H. Zhang, Y.-B. Li, H.-Y. Lin, L. Li, J.-J. Wu, C.-L. Liu, Z.-M. Ye, S.-C. Xiang, B.-L. Chen and Z.-J. Zhang, *Chem*, 2023, **9**, 3532.
12. H. Yao, Y.-M. Wang, M. Quan, M. U. Farooq, L.-P. Yang and W. Jiang, *Angew. Chem. Int. Ed.*, 2020, **59**, 19945.
13. Z.-H. Qiu, J.-H. Li, B.-X. He, P.-Q. Liao, M.-Y. Zhou, P.-X. Li, R.-B. Lin, J.-P. Zhang and X.-M. Chen, *J. Mater. Chem. A*, 2024, **12**, 13240.
14. Y. Han, Y.-L. Chen, Y.-J. Ma, J. Bailey, Z. Wang, D. Lee, A. M. Sheveleva, F. Tuna, E. J. L. McInnes, M. D. Frogley, S. J. Day, S. P. Thompson, B. F. Spencer, M. Nikiel, P. Manuel, D. Crawshaw, M. Schröder and S.-H. Yang, *Chem*, 2023, **9**, 739.
15. C.-R. Ye, W.-J. Wang, W. Chen, Y.-H. Xiao, H.-F. Zhang, B.-L. Dai, S.-H. Chen, X.-D. Wu, M. Li and X.-C. Huang, *Angew. Chem. Int. Ed.*, 2021, **60**, 23590.
16. A. A. Lysova, D. G. Samsonenko, P. V. Dorovatovskii, V. A. Lazarenko, V. N. Khrustalev, K. A. Kovalenko, D. N. Dybtsev and V. P. Fedin, *J. Am. Chem. Soc.*, 2019, **141**, 17260.
17. G. Li, C.-F. Zhu, X.-B. Xi and Y. Cui, *Chem. Commun.*, 2009, DOI: 10.1039/b901574d.
18. Y. Zhao, T. Irie, D. Wen, H. Mabuchi, K. Sasaki, M. Nozaki, R. Tomioka, W.-D. Zhu, S. Das, T. Ben and Y. Negishi, *ACS Materials Lett.*, 2024, **6**, 3063.
19. J.-H. Chang, F.-Q. Chen, H. Li, J.-Q. Suo, H.-R. Zheng, J. Zhang, Z.-T. Wang, L.-K. Zhu, V. Valtchev, S.-L. Qiu and Q.-R. Fang, *Nat. Commun.*, 2024, **15**, 813.
20. J. Yan, H.-Y. Sun, Q.-L. Wang, L. Lu, B. Zhang, Z.-G. Wang, S.-W. Guo and F.-L. Han, *New J. Chem.*, 2022, **46**, 7580.

21. Y. Fan, X. Tang, J. Hu, Y. Ma, J. Yang, F. Liu, X. Yi, Z. Liu, L. Song, A. Zheng and Y. Ma, *Nat Commun*, 2024, **15**, 7961.
22. A. Valencia, R. Muñiz-Valencia, S. G. Ceballos-Magaña, C. K. Rojas-Mayorga, A. Bonilla-Petriciolet, J. González and I. A. Aguayo-Villarreal, *Environ. Technol.Inno.*, 2022, **25**, 102076.